NAVAL
POSTGRADUATE
SCHOOL

MONTEREY, CALIFORNIA

THESIS

BATTLE DAMAGE ASSESSMENT USING INVERSE
SYNTHETIC APERTURE RADAR (ISAR)

by

Lim Kian Guan

December 2004

Thesis Advisor:	Brett H. Borden
Co-Advisor:	Donald L. Walters

Approved for public release; distribution is unlimited

THIS PAGE INTENTIONALLY LEFT BLANK

REPORT DOCUMENTATION PAGE			*Form Approved OMB No. 0704-0188*
Public reporting burden for this collection of information is estimated to average 1 hour per response, including the time for reviewing instruction, searching existing data sources, gathering and maintaining the data needed, and completing and reviewing the collection of information. Send comments regarding this burden estimate or any other aspect of this collection of information, including suggestions for reducing this burden, to Washington headquarters Services, Directorate for Information Operations and Reports, 1215 Jefferson Davis Highway, Suite 1204, Arlington, VA 22202-4302, and to the Office of Management and Budget, Paperwork Reduction Project (0704-0188) Washington DC 20503.			
1. AGENCY USE ONLY *(Leave blank)*	**2. REPORT DATE** December 2004	**3. REPORT TYPE AND DATES COVERED** Master's Thesis	
4. TITLE AND SUBTITLE: Battle Damage Assessment Using ISAR		**5. FUNDING NUMBERS**	
6. AUTHOR(S) LIM KIAN GUAN			
7. PERFORMING ORGANIZATION NAME(S) AND ADDRESS(ES) Naval Postgraduate School Monterey, CA 93943-5000		**8. PERFORMING ORGANIZATION REPORT NUMBER**	
9. SPONSORING /MONITORING AGENCY NAME(S) AND ADDRESS(ES) N/A		**10. SPONSORING/MONITORING AGENCY REPORT NUMBER**	
11. SUPPLEMENTARY NOTES The views expressed in this thesis are those of the author and do not reflect the official policy or position of the Department of Defense or the U.S. Government.			
12a. DISTRIBUTION / AVAILABILITY STATEMENT Approved for public release; distribution is unlimited		**12b. DISTRIBUTION CODE**	
13. ABSTRACT (maximum 200 words) An imaging radar, like ISAR, offers a combatant the capability to perform long range surveillance with high quality imagery for positive target identification. Extending this attractive feature to the battle damage assessment problem (BDA) gives the operator instant viewing of the target's behavior when it is hit. As a consequence, immediate and decisive action can be quickly taken (if required). However, the conventional Fourier processing adopted by most ISAR systems does not provide adequate time resolution to capture the target's dynamic responses during the hit. As a result, the radar image becomes distorted. To improve the time resolution, time-frequency transform (TFT) methods of ISAR imaging have been proposed. Unlike traditional Fourier-based processing, TFT's allows variable time resolution of the entire event that falls within the ISAR coherent integration period to be extracted as part of the imaging process. We have shown in this thesis that the use of linear Short Time-Frequency Transforms allows the translational response of the aircraft caused by a blast force to be clearly extracted. The TFT extracted images not only tell us how the aircraft responds to a blast effect but also provides additional information about the cause of image distortion in the traditional ISAR display.			
14. SUBJECT TERMS ISAR, Radar Imaging, Time Frequency, Image processing, High Resolution Radar, Battle Damage Assessment, BDA.			**15. NUMBER OF PAGES** 117
			16. PRICE CODE
17. SECURITY CLASSIFICATION OF REPORT Unclassified	**18. SECURITY CLASSIFICATION OF THIS PAGE** Unclassified	**19. SECURITY CLASSIFICATION OF ABSTRACT** Unclassified	**20. LIMITATION OF ABSTRACT** UL

THIS PAGE INTENTIONALLY LEFT BLANK

BATTLE DAMAGE ASSESSMENT USING INVERSE SYNTHETIC APERTURE RADAR (ISAR)

Lim Kian Guan
Major, Republic of Singapore Navy
B.Eng. (Hon), Nanyang Technological University, 1999

Submitted in partial fulfillment of the
requirements for the degree of

MASTER OF SCIENCE IN COMBAT SYSTEMS TECHNOLOGY

from the

**NAVAL POSTGRADUATE SCHOOL
December 2004**

Author: Lim Kian Guan

Approved by: Brett H. Borden
                 Thesis Advisor

                 Donald L. Walters
                 Co-Advisor

                 James Luscombe
                 Chairman, Department of Physics

THIS PAGE INTENTIONALLY LEFT BLANK

ABSTRACT

An imaging radar, like ISAR, offers a combatant the capability to perform long range surveillance with high quality imagery for positive target identification. Extending this attractive feature to the battle damage assessment problem (BDA) gives the operator instant viewing of the target's behavior when it is hit. As a consequence, immediate and decisive action can be quickly taken (if required). However, the conventional Fourier processing adopted by most ISAR systems does not provide adequate time resolution to capture the target's dynamic responses during the hit. As a result, the radar image becomes distorted. To improve the time resolution, time-frequency transform (TFT) methods of ISAR imaging have been proposed. Unlike traditional Fourier-based processing, TFT's allows variable time resolution of the entire event that falls within the ISAR coherent integration period to be extracted as part of the imaging process. We have shown in this thesis that the use of linear Short Time-Frequency Transforms allows the translational response of the aircraft caused by a blast force to be clearly extracted. The TFT extracted images not only tell us how the aircraft responds to a blast effect but also provides additional information about the cause of image distortion in the traditional ISAR display.

THIS PAGE INTENTIONALLY LEFT BLANK

TABLE OF CONTENTS

ix

THIS PAGE INTENTIONALLY LEFT BLANK

LIST OF FIGURES

LIST OF TABLES

THIS PAGE INTENTIONALLY LEFT BLANK

ACKNOWLEDGMENTS

THIS PAGE INTENTIONALLY LEFT BLANK

I.   INTRODUCTION

A.   ISAR FOR BATTLE DAMAGE ASSESSMENT (BDA)

A radar target[1] image is generated from the reflectivity data collected by a radar platform as the target is observed from a set of viewing angles. For Synthetic Aperture Radar (or SAR), the radar platform moves to give the different target viewing angles, whereas Inverse Synthetic Aperture Radar (ISAR) makes use of the target's angular rotations such as roll, pitch and yaw to collect the viewing angles for image generation.

ISAR imaging opens up the new possibility of using radar measurements to construct high quality images for target recognition purposes while the target (usually aircraft and ships) is moving and the radar platform remains essentially stationary[2]. Operationally, ISAR offers enhanced target recognition at ranges that are often not achievable by electro-optic systems or Forward Looking Infrared (FLIR) alone. An extension of this long-range target recognition capability of the ISAR, apart from deploying for surveillance purpose, is to use it to perform Battle Damage Assessment (BDA).

The significant advantage of using ISAR for BDA (over other methods) is its ability to provide the operator instantaneous viewing, in highly resolved detail, of the behavior of the target as a kinetic energy weapon hits it. This gives the operator immediate evaluation of the extent of the damage caused by the hit. Follow-up counter actions can be quickly taken if needed (all being performed beyond the target's weapon range).

B.   RADAR TARGET IMAGING USING ISAR

To construct a radar image from the reflectivity data, most ISAR systems process the data by performing a two dimensional (2D) Fast Fourier Transform

---

[1] The target can be any object of interest to the radar operator.

[2] The platform can be in motion but its motion has to be accurately measured (usually by the combination of Inertial Navigation System (INS) and Global Positioning System (GPS), and compensated accordingly.

(FFT); the first FFT generates the synthetic range profile of the target, and the second FFT extracts the Doppler information for each range cell. Ideally, the resultant 2D Range-Doppler plot following this process would closely resemble an outline of the target, arising from the various scattering points around the target. The quality of the generated ISAR image is directly related to the resolution imposed by the processing system. High range resolution can be achieved through pulse compression, and Stepped Frequency Waveforms (SFW) are the most common methods used today. High cross-range resolution depends strongly on the variation in viewing angles (equivalently Doppler resolution) which, in turn, increases with higher angular rate of target rotation and target dwell time.

However, a subtlety that affects the quality of the ISAR image results from the requirement of minimum variation in the range over the different viewing angles between the radar platform and the target for cross-range synthesis. Significant variation in range (due to the presence of translational velocity components, non-linear or large variations in angular velocity, or combination of both) will introduce an additional quadratic phase error that tends to distort or blur (known also as the defocusing effect) the image during the signal processing stage. This phenomenon is called "Range Walk" by the SAR imaging community, and it acts to impose an upper limit on the effective observed target rotation interval and—because this interval is determined by rotation rate—range walk also bounds the integration time.

Normally, if the radial velocity remains essentially constant, the motion of the target can be accurately estimated (and compensated for) to reduce the effects of range walk. The angular velocity, on the other hand, is needed for ISAR imaging and is generally assumed to be constant and reasonably small over the entire data integration time. In most (aircraft or ship) target's roll, pitch and yaw behaviors, this is approximately valid for the observation period. The converse is not true though if the target experiences any acceleration.

C. RESPONSE OF TARGET BEING HIT

While the target is being hit, the blast force from the explosion of the weapon—or weapon impact itself—acting on the target structure will cause it to undergo translational and rotational motions, as well as structural vibration. The time duration of this force acting on the target is often very short (on order of milliseconds) but the impulse is large enough to cause significant alterations in both radial and angular velocity of the target. As a consequence of this short impulse period, the radar may not have adequate time to compensate for these changes in velocities and hence errors are introduced into the image processing. These errors could account for the distortion in most ISAR image observed when the target is being hit.

In addition to the translational, rotation and vibration effects, the sharp and high velocity fragments from the weapon as it explodes, or possible a Kinetic Energy (KE) round itself, are likely to penetrate the target causing it to break up. The smaller broken target pieces now begin to scatter and reflect electromagnetic signals back to the radar as they move at much higher velocities (from the energy acquired) than the target (which has larger mass). The returned scattered EM signal from these pieces can behave like point scatterers, dihedral, trihedral or multi-facet corner reflectors, or specular reflectors depending on the dynamic nature of the break-up process. It is difficult to predict target structure changes without an in-depth analysis based on explosive and structural impact studies. In most cases, numerical simulations such as finite element analysis are often used in these studies and the results obtained are only specific to the particular scenario defined. Due to time constraints, this topic will not be pursued in the thesis work.

D. JOINT TIME-FREQUECY METHOD OF ISAR IMAGING FOR BDA

Time-frequency methods for signal analysis (also known as the Time-Frequency Transform or TFT) are similar to conventional Fourier Transform (FT) schemes except that the FT is taken after the auto-correlation of the signal with a

weighted window function. The advantage of this analysis method is that it allows decomposition of the frequency spectrum of time-varying signals in shorter window time frames, and provides an added dimension for examining the dynamic behavior of the signal as it varies over time. The size and shape of the weighting window function can be altered to fit the specific analysis requirement for the signal.

Time-frequency methods in signal analysis have aroused much interest in the signal processing community. The initial application was in spectrogram analysis of complex human speech. However, in recent years, further extension of this time-frequency method to ISAR was actively advocated by Chen [2] and Jae and Thomas and Flores [3] — particularly in the area of image generation, motion compensation and micro-Doppler target vibration studies. In image generation, Chen [2] has reportedly used the TFT to construct ISAR image of targets with high rotation rate by helping to overcome the migration of individual scattering points from one range cell to another. Both Jae, Thomas and Flores [3] and Chen [2] have also proposed the use of TFTs to resolve multiple targets appearing in ISAR images.

So far, the possibility of using the TFT to examine the dynamic behavior of a target in an ISAR image as the target is being acted upon by an impulse blast force has yet to be explored by other TFT-centered research efforts. If the target is assumed to be a rigid body, it would experience sudden translational and rotational motion variation under blast wave loading. These motions will be measured during the data collection process if the radar is continuously staring at the target. This thesis aims to apply the appropriate TFT window function to the collected ISAR data and demonstrate the possibility of extracting these target motions using TFT methods of image construction.

E.   THESIS OUTLINE

The thesis is organized in the following manner:

Chapter II serves to develop the theory of ISAR image processing. This chapter will touch on how high quality image resolution is achieved, and the conditions necessary to maintain the quality of the image generated.

In Chapter III, the effects of blast waves interacting with a target are described with the goal of modeling and simulation. The subject target for this study is an aircraft which is treated as a rigid body to simplify the analysis. The translational and rotational motions resulting from force interaction are examined.

Chapter IV introduces the Time-Frequency Transform (TFT) Method of analysis, and how it can be applied to ISAR signal processing and image generation. The discussion in this chapter is largely based on the work of Chen [2] in TFT method for ISAR imaging and Jae and Thomas and Flores [3] for motion compensation.

To demonstrate the feasibility of using TFT methods for ISAR imaging, and their advantage over conventional FFT based methods for BDA (oweing to the dynamic behavior of the aircraft as it is hit), a simple simulation program is developed. Chapter V describes how this program is put together for modeling the radar target returns from an aircraft, the effect of the blast loading on the aircraft and the construction of ISAR images using TFT concepts. This chapter also discusses the parameters and conditions used in the simulation.

Chapter VI follows on to discuss the results of the simulation and its significance.

Chapter VII is the concluding chapter and summarizes the major findings of the thesis work and provides recommendations for similar future work.

THIS PAGE INTENTIONALLY LEFT BLANK

II. INVERSE SYNTHETIC APERTURE RADAR (ISAR) THEORY AND SIGNAL PROCESSING

A. RADAR IMAGING AND ITS ASSOCIATED RESOLUTIONS

Radar has long been recognized for its ability to "detect, locate and identify targets at great distance and in all kind of weather conditions" [1] and, to date, it is hardly matched by other sensors. Compared to Infrared (IR), visible or Ultra-violet sensors, the longer wavelengths (by four to six orders of magnitude) allow the radar energy to propagate through most of the atmosphere with little loss, even in poor weather conditions. However, the long wavelengths limit the radar's imaging resolution, which is proportional to the ratio of the wavelength to the aperture size, and hence affects the image quality. To achieve the fine image resolution in optics, a lens system with aperture size of up to several centimeters is adequate. But a radar system would require an antenna aperture diameter to stretch tens of kilometers to attain the same resolution. Thus, alternate methods to accomplish this must be found.

Inverse Synthetic Aperture Radar (ISAR) combines the use of pulse compression, high Pulse Repetition Frequency (PRF) and the target motions (particularly its angular rotation) to generate high range and cross-range resolution target images. Range resolution is associated with the width of the target pulse in the time domain. Hence, narrower pulses will have better resolution. But such radar systems require higher peak power to ensure enough energy returned from the target for signal processing. To mitigate this, pulse compression is mostly employed and for ISAR a common technique uses Stepped Frequency Waveforms (SFW). High cross-range resolution can be achieved by observing the phase variations of the signals returned from different target viewing angles over a coherent processing or integration period. It can be shown, under rather stringent conditions (in subsequent sections), that the changes in phase due the rotation of the target can be mapped in one-to-one correspondence to the cross-range position of the target scattering points.

B. ISAR SYSTEM ARCHITECTURE

Figure 1 below shows the architecture of a simple SFW ISAR system. At the RF stage, a series of high PRF narrow pulses is used to modulate the RF carrier that varies in frequency steps of Δf at every pulse interval, T_2, which is reciprocal to the PRF. A burst of transmitted pulses consists of N stepped frequency pulses varying from f_c to $f_c + (n-1)\Delta f$, where $n = 1, 2, ..., N.$. For ISAR image processing, M bursts are required to form an image. The size of the image is thus determined by the $M \times N$ sequence of the pulses, and the integration time, T, needed to construct the image (if we ignored the processing delays) is then $T = M \times N \times T_2$. The $M \times N$ SFW pulse sequence represents the Doppler-Range mapping for the image.

f_I – Intermediate frequency
f_c – Carrier Frequency
Δf – Stepped frequency
$n = 1, 2, ..., N$
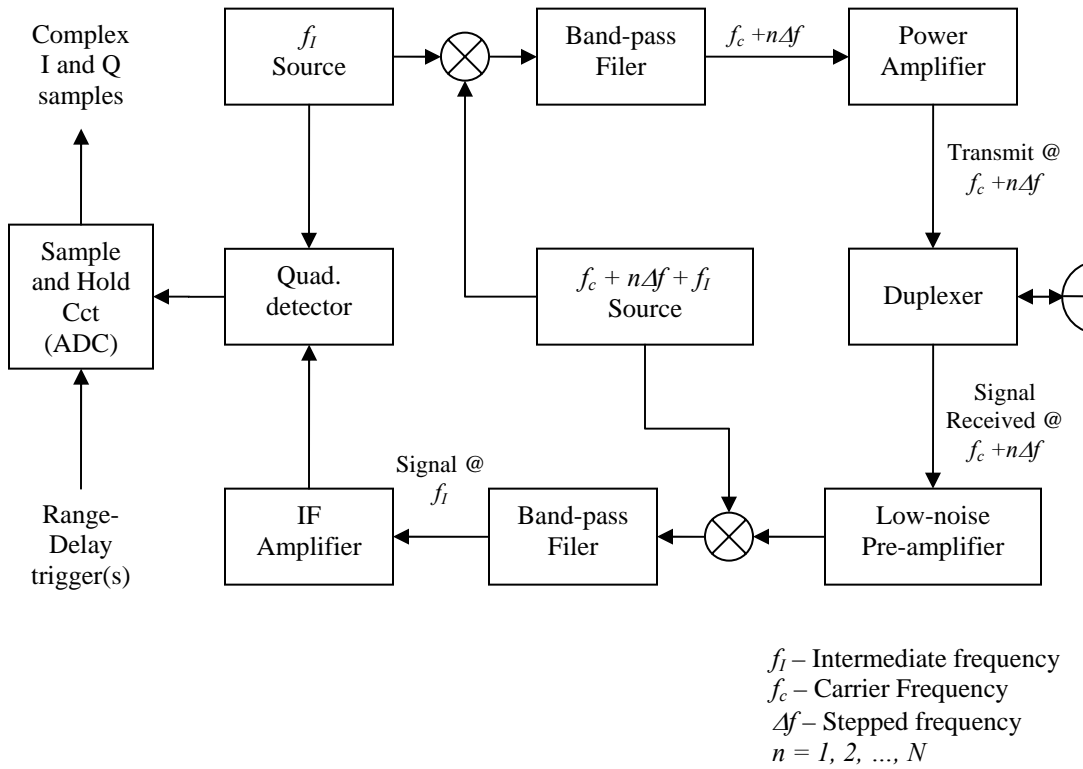
(a) RF transmission and detection stages (After: Figure 5.2(b), pp 202, Wehner [4])

8

Complex I and Q samples

Range Alignment and Tracking

Doppler Tracking and Motion Compensation

Range Cells

1
2
3

N

M Time Histories

FFT

FFT

Range – Doppler ISAR Image (M x N size)
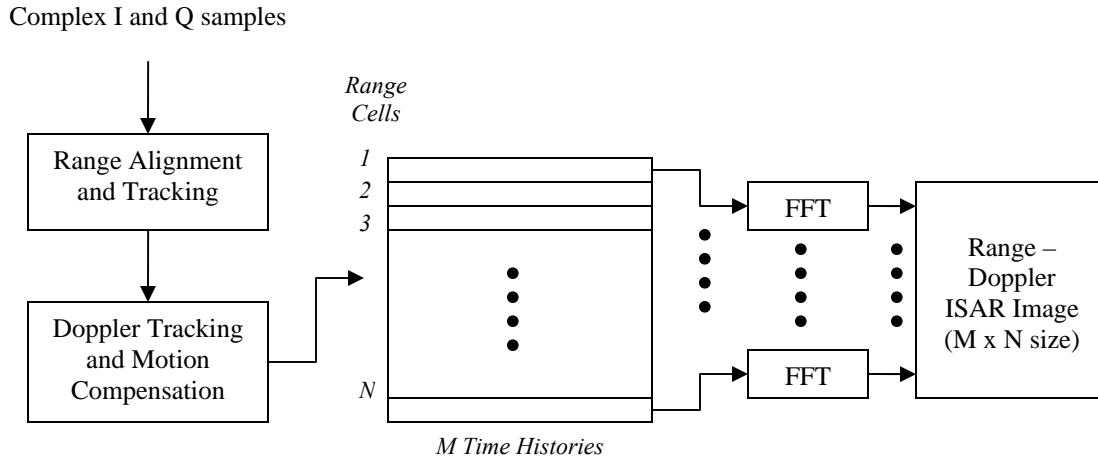
(b) Signal and image processing stages (After: Figure 5.2, pp 100, Chen [2])

Figure 1   A simple illustration of SWF ISAR architecture.

The returned echo signal captured by the receiver immediately after each pulse transmission is down-converted to an intermediate frequency (IF) and passed along for quadrature detection. The quadrature detector detects the baseband signal in the form of in-phase (I) and quadrature phase (Q) signals. These signals are then sampled and held as an *M x N* data array for signal processing. The sampled output data represents the time-history of the target's reflectivity in the frequency domain.

At the signal processing stage shown in Figure 1(b), corrections for radar system "phase and amplitude ripples" (Wehner [4]) are first applied, followed by range alignment, translational and rotational motion compensations in the form of range and Doppler tracking. Motion compensations are employed to minimize the induced quadratic phase error and hence "Range Walk" effect. The actual image construction begins with the synthetic range profile processing which is simply formed by taking an inverse Fourier transform of the N pulses for each m burst where $m = 1, 2, ..., M$. Cross-range information is then extracted by another Fourier process – a direct Fourier transform this time – along the column of M

bursts for each n range cell index. In practice, the synthetic range profile and cross-range (Doppler history) information are simultaneously processed by taking a two-dimensional Fast Fourier Transform[3] (FFT) of the compensated $M \times N$ data array to lessen the computation load.

C.   THEORY OF MOVING TARGET IMAGING IN ISAR
1.   ISAR Geometry and its Relationship with the Returned Signal

For illustration purposes, consider a simplified two-dimensional (2D) geometry between the radar and an airborne target as shown below in Figure 2. The aircraft is assumed to have translational and rotational motion only in the two-dimensional plane relative to a stationary radar platform. It can be easily extended to the actual three-dimensional case to include the effect of the motions along and about the other axes with some careful considerations.
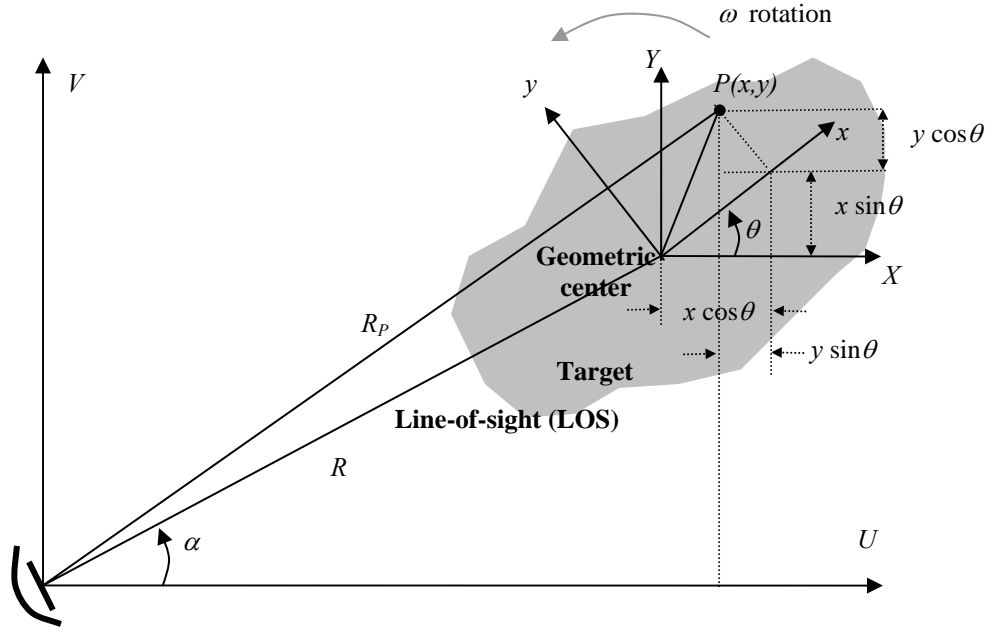
Figure 2   ISAR geometry in two-dimensional space.

(After: Figure 5.1, pp95, Chen [2])

---

[3] It can be shown that the process of IDFT and subsequently DFT is equivalent to taking a two-dimensional FFT with the exception of a phase factor in front. In most radar signal processing, we can ignore this phase factor since our interest is largely on the power spectral density or absolute intensity of the returns.

Following Chen [2], we designate the radar to be located at the origin of the U-V coordinate system, known as radar coordinates. The target can be described by a collection of scattering points (or, "scattering centers") in its own reference frame, x-y, known as the target coordinates. The center of rotation of the target is located at the origin of this x-y coordinate system. To describe the rotation of the target independent of the target scattering center distribution in x-y coordinates, another reference coordinate system denoted as X-Y is introduced with its origin coincident with the target coordinates. The two axes in X-Y are parallel to U and V axes respectively so that a pure translational transformation can be used to describe their relationship. Then, it follows that the transformation of x-y reference to X-Y coordinate can be described by a pure rotation. Also, to simplify the illustration further, we assume $\alpha = 0$ (the radar target line of sight (LOS) is along the $U - axis$ of the radar reference).

Assume that at $t = 0$ the target range (the distance from the radar to the center of rotation of the target) is R. Hence, the distance between the radar and a scattering point, $P(x,y)$, can be expressed as

$$
\begin{aligned}
R_p &= \left[\left(R + x\cos\theta_0 - y\sin\theta_0 \right)^2 + \left(y\cos\theta_0 + x\sin\theta_0 \right)^2 \right]^{1/2} \\
&= \left[R^2 + x^2 + y^2 + 2R\left(x\cos\theta_0 - y\sin\theta_0 \right) \right]^{1/2} \\
&\cong R + x\cos\theta_0 - y\sin\theta_0
\end{aligned}
\tag{2.1}
$$

where θ_o is the initial target rotation angle.

If the target possesses both translational and rotational motion described by an initial angular rotation rate (ω), initial radial velocity (V_t) and its higher order initial angular (γ) and radial acceleration (a_t) and so on, the target range and the rotation angle as a function of time are then

$$
R(t) = R_0 + V_t t + \frac{1}{2} a_t t^2 + ...
\tag{2.2}
$$

$$\theta(t) = \theta_0 + \omega t + \frac{1}{2}\gamma t^2 + \dots \tag{2.3}$$

Thus, at time t, (2.1) becomes,

$$R_p \cong R(t) + x\cos\theta(t) - y\sin\theta(t) \tag{2.4}$$

For simplicity, if we assume the reflectivity function of target, $\rho(x,y)$, to be a pure function of the target geometry and that it does not change with the above parameters, then the base-band of the returned signal from the scattering point, $P(x,y)$, will consist simply of the product of the reflectivity function and the phase variation due to the distance, R_P:

$$s_P(t) = \rho(x,y)\exp\left\{-j2\pi f_c \frac{2R_P(t)}{c}\right\} = \rho(x,y)\exp\left\{-j\psi(R_{Pt})\right\} \tag{2.5}$$

2.   Signal Representation

We next look at the signal representation of the returned echoes for the imaging process. At any given time t, the radar receives a collection of returned signals from all the scattering centers of the target. The received base-band signal can be described as a superposition of these signals:

$$s_R(t) = \int_{-\infty}^{\infty}\int_{-\infty}^{\infty} \rho(x,y)\exp\left\{-j2\pi f_c \frac{2R_P(t)}{c}\right\} dxdy \tag{2.6}$$

Substituting (2.4) into (2.6), we obtain

$$s_R(t) = e^{-j4\pi f_c \frac{2R(t)}{c}} \int_{-\infty}^{\infty}\int_{-\infty}^{\infty} \rho(x,y)\exp\left\{-j2\pi\left[xf_x(t) + yf_y(t)\right]\right\} dxdy \tag{2.7}$$

where

$$f_x(t) = \frac{2f_c}{c}\cos\theta(t) \text{ and } f_y(t) = -\frac{2f_c}{c}\sin\theta(t)$$

Apart from the pre-factor (due to the translational motion) in (2.7), the base-band received signal at a given time can be seen to be a two-dimensional Fourier transform of the target reflectivity function. This is the basis for the

12

method of extracting the target reflectivity information by applying a direct two-dimensional inverse Fourier transform or FFT on the collected data.

3. ISAR Data Collection and Processing

In almost all ISAR systems, the signal processing is performed discretely. To gain more intuition into this procedure, it is convenient to consider the discrete representation of the base-band signal rather than its continuous form. For our earlier discussion on ISAR architecture, we set the frequency dependence for each m burst of pulses to increase from f_c in steps of Δf from pulse to pulse.

$$f_n = f_c + (n-1)\Delta f \qquad where\ n = 1,\ 2,\ ...,\ N \qquad (2.8)$$

Also, the base-band signal will be time-sampled at the interval corresponding to the pulse interval (T_2) plus the range of the target center. Accordingly (Jae, Thomas and Flores [3]), the discrete sampled frequency and time can be represented as

$$t_{m,n} = \left[n+(m-1)N\right]T_2 + \frac{2R_0}{c} \qquad where\ m =1,\ 2,\ ...,\ M \qquad (2.9)$$

Therefore, (2.2), (2.3) and (2.7) can be expressed in terms of (2.8) and (2.9) as

$$s_R(m,n) = e^{-j4\pi f_n \frac{2R(m,n)}{c}} \int_{-\infty}^{\infty}\int_{-\infty}^{\infty} \rho(x,y)\exp\left\{-j2\pi\left[xf_x(m,n)+yf_y(m,n)\right]\right\}dxdy$$

$$R(m,n) = R_0 + V_t t_{m,n} + \tfrac{1}{2}a_t t_{m,n}^2 + ...$$

$$\qquad (2.10)$$

$$f_x(m,n) = \frac{2f_n}{c}\cos(\theta_0 + \omega t_{m,n} + \tfrac{1}{2}\gamma t_{m,n}^2 + ...)$$

$$f_y(m,n) = -\frac{2f_n}{c}\sin\theta(\theta_0 + \omega t_{m,n} + \tfrac{1}{2}\gamma t_{m,n}^2 + ...)$$

13
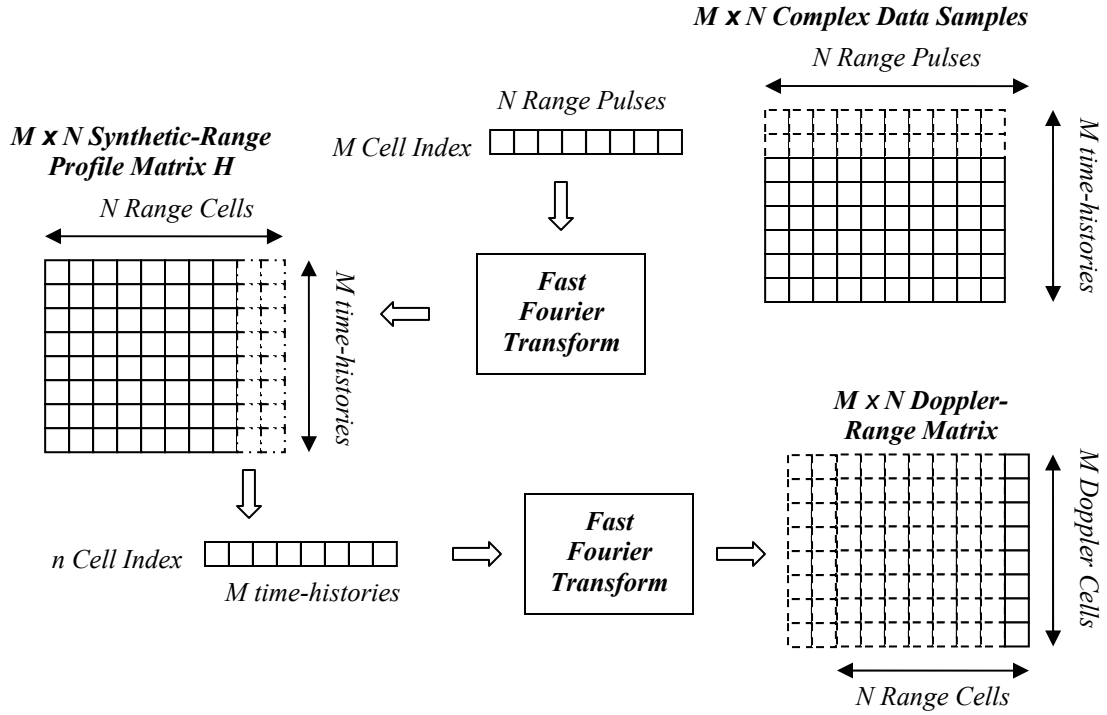
Figure 3   Row-column decomposition for synthetic ISAR imaging.

Figure 3 shows the image-processing sequence for the M x N ISAR complex-valued sampled data matrix array. The image construction process begins with synthetic range profile extraction by an Inverse Discrete Fourier Transform (IDFT). This operation on each m and n point in the M x N matrix is given as such (Jae, Thomas and Flores [3]).

$$h(m,n) = \frac{1}{N} \sum_{i=0}^{N-1} s_R(m,i) e^{j\frac{2\pi n i}{N}} \qquad where\ n = 1,\ 2,\ ...,\ N \qquad (2.11)$$

The resultant $M\ x\ N$ matrix is analyzed by another Fourier process – the Discrete Fourier Transform (DFT) – to gather the cross-range information. If we denote the output of the transformed point in the resultant $M\ x\ N$ matrix by $D(m,n)$, we obtain

$$D(m,n) = \frac{1}{M} \sum_{k=0}^{M-1} h(k,n) e^{-j\frac{2\pi km}{M}} \qquad where\ m = 1,\ 2,\ ...,\ M \qquad (2.12)$$

14

The magnitude of the elements of resultant complex matrix forms the ISAR image.

D. ACHIEVING HIGH RANGE RESOLUTION THROUGH STEPPED FREQUENCY WAVEFORM (SFW) SIGNAL PROCESSING

Most radars today attain high range resolution through various forms of pulse compression. For a pulse compression radar, the achievable range resolution is inversely proportional to the system bandwidth, and thus, to gain high resolution the entire radar system — from transmitter through receiver and including data collection — must possess the large bandwidth associated with the desired resolution. Designing a radar to have such wide bandwidth at all its stages can be an expensive and a rather complex issue.

SFW avoids this stringent requirement by simply varying the carrier frequency prior to transmission in N frequency steps associated with the desired range resolution. The same stepped carrier frequency is also used as the reference to the mixer to down-convert the returned signal back to the IF stage. Consequently, the IF stage, the detection stage and later processing stages no longer require large bandwidth to maintain the resolution. In addition to relaxing the wide bandwidth requirement for the other radar system stages, the SFW technique also has the advantage that the returned base-band signal is a spectral representation of the target's reflectivity with range-invariant magnitude. This is a desirable property for range tracking (Wehner [4]).

In doing so, on the other hand, the returned signal no longer preserves its direct phase relationship with the range profile of the target. To obtain the target range profile an inverse Fourier transform is needed to get back the target range profile. This process is known as synthetic range-profile processing.

1. Synthetic Range Profile Processing

Figure 4 shows an SFW transmission and its associated returned echo pulse. From Wehner [4], each received echo pulse is equivalent to a replica of

the transmitted SFW with a time delay of $\tau(t) = 2 (R_p - v_t t) / c$. After passing through RF, IF, and the quadrature detection stage, the carrier component is removed leaving only the base-band signal with a phase output of $\Psi_n(t) = 2\pi f_n \tau(t)$. This signal is, in turn, sampled at $S_n = nT_2 + \tau_r + 2R_p / c$ where τ_r is the receiving system transfer delay, R_p represents the range of a point target (it is often estimated through range alignment), and c is the velocity of wave propagation (Wehner [4]).
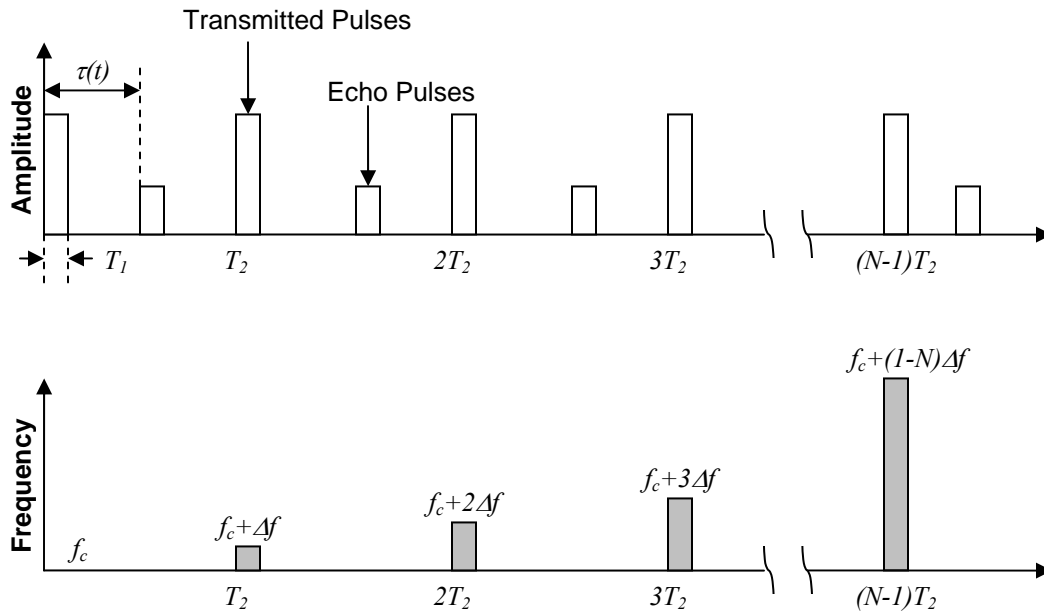
Figure 4   SFW Pulse and echo pulses.
(After: Figure 5.5, pp 204, Wehner [4])

The sampled output from both the I- and Q- channels can now be written in complex form where A_n is the signal amplitude (which is usually normalized for ease of illustration (Wehner [4])):

$$G_n = A_n e^{j\psi_n} \tag{2.13}$$

and

16

$$\psi_n = -2\pi f_n \left[\frac{2R_p}{c} - \frac{2v_t}{c} \left(nT_2 + \tau_r + \frac{2R_p}{c} \right) \right]$$ (2.14)

The N sampled output data for each burst are then Fourier transformed by IDFT or FFT to obtain a series of synthetic complex range-profiles of the target, H_l, where l is the slant-range position. Following Wehner [4], the IDFT is expressed as

$$H_l = \sum_{i=0}^{N-1} G_i e^{j(2\pi/N)li}, \qquad 0 \le l \le N-1$$ (2.15)

Putting (2.13) and (2.14) into (2.15), and assuming zero target velocity, the normalized synthetic response of the target is

$$H_l = \sum_{i=0}^{N-1} \exp j \left(\frac{2\pi}{N} li - 2\pi f_i \frac{2R_p}{c} \right)$$ (2.16)

Replacing $f_i = f_c + i\Delta f$ in (2.16), this becomes

$$H_l = \exp\left(-j2\pi f_c \frac{2R_p}{c} \right) \sum_{i=0}^{N-1} \exp j \left[\frac{2\pi i}{N} \left(\frac{-2NR_p\Delta f}{c} + l \right) \right]$$ (2.17)

This equation can be further simplified using the same analysis as for antenna array theory (from Wehner [4]) to become

$$H_l = \exp\left(-j2\pi f_c \frac{2R_p}{c} \right) \frac{\sin \pi y}{\sin \dfrac{\pi y}{N}} \exp\left(j \frac{N-1}{2} \frac{2\pi y}{N} \right)$$ (2.18)

where

$$y = \frac{-2NR_p\Delta f}{c} + l$$ (2.19)

It is noted for (2.18) that the resultant response represents the range point spread function (PSF) of the target in the range cell index l where the highest peak indicates the range position of the target point. The collection of all the range cell indices from $l = 0, 1, ..., N - 1$ is known to be the synthetic range profile of the target.

2.   Unambiguous Range and Range Resolution

From both (2.18) and (2.19), the peak response occurs when $y = 0, +/-N, +/-2N, +/-3N,...$ corresponding to the range given by (Wehner [4])

$$R_p = \frac{cl_o}{2N\Delta f}, \frac{c(l_o \mp N)}{2N\Delta f}, \frac{c(l_o \mp 2N)}{2N\Delta f}, ...$$

(2.20)

The unambiguous range length is then:

$$\Delta R = \frac{c(l_o \mp N)}{2N\Delta f} - \frac{cl_o}{2N\Delta f} \text{ or } \frac{c(l_o \mp 2N)}{2N\Delta f} - \frac{c(l_o \mp N)}{2N\Delta f} \text{ or} ... = \frac{c}{2\Delta f}$$

(2.21)

and the range resolution (using Rayleigh's resolution distance criteria[4]) corresponds to the width of the PSF of each target point, which is

$$\Delta R_p = \frac{c}{2N\Delta f}$$

(2.22)

Both parameters depend on the frequency step size but the range resolution can be enhanced by placing a higher number of pulses within each burst.

3.   Effect of Target Velocity

In the above, the synthetic range response of the target is obtained for a target with zero velocity. However, if target linear velocity is present, the synthetic range response becomes

$$H_l = \sum_{i=0}^{N-1} \exp j \left\{ \frac{2\pi}{N} li - 2\pi f_i \left[\frac{2R_p}{c} - \frac{2v_t}{c} \left(iT_2 + \tau_r + \frac{2R_p}{c} \right) \right] \right\}$$

(2.23)

In this case, the range resolution can no longer be simply expressed as in (2.22). Moreover, analytically deriving the range resolution ΔR_p from (2.23) is also not a trivial problem. Through numerical solution, Wehner [4] has reportedly shown

---

[4] Rayleigh criterion defines the resolution between two point spread functions to be the overlap of one highest maximum peak with the first minimum of the other highest peak. For a *sinc* function, this occurs at the first null in which the argument in the sinc function is π.

that the higher velocity can cause the width of the PSF to broaden, thus resulting in poorer range resolution.

4.   Range Offset and Range Walk

The presence of nonzero translational target velocity has the consequence of creating range offset and range walk effects, and therefore distorts the radar image. When ISAR constructs a radar image from the collected data, it presumes that the range of every target scattering point does not vary during the integration time interval. Range offset and range walk result when this presumed condition fails to be true due to the presence of radial velocity components. The extent of the range walk and range offset can be quantified by the number of cells (ΔN) that the range is shifted over the entire time integration period (T) for the radar time delay resolution of $\Delta t = 1 / N\Delta f$. Thus, from Wehner [4], ΔN is expressed as

$$\Delta N = \frac{\delta\tau}{\Delta t} = N\Delta f\,\delta\tau \tag{2.24}$$

where $\delta\tau$ represents the time delay shift of the target due to the presence of radial velocity over the period where $\delta\tau$ is evaluated.   This delay shift is determined from the total group delay and can be derived by taking the derivative of (2.14) and subtracting the time delay $2R_p / c$. In general, $\delta\tau$ is cumulative over the number of bursts, m, and is given by Wehner [4] as

$$\delta\tau = -\frac{2v_t}{c\Delta f}\left[f_c T_2 + \Delta f\left(\tau_r + \frac{2R}{c} + NmT_2 \right)\right] \tag{2.25}$$

Putting (2.25) into (2.24), and noting that $NmT_2 >> \tau_r + 2R / c$ is true in most cases, we obtain

$$\Delta N \approx -\frac{2(NT_2)}{c}\left(f_c + Nm\Delta f \right)v_t \tag{2.26}$$

For the entire image frame time, we let $m = M$, and obtain

$$\Delta N \approx -\left[\frac{2(NT_2)}{c} f_c + \frac{2M(NT_2)N\Delta f}{c} \right] v_t \qquad (2.27)$$

The first term in (2.27) represents the range offset which increases with higher values of N, higher carrier frequency and lower PRF. The second term is the result known as range walk and is cumulative from profile to profile (burst to burst) depending on size of M. Unlike range offset, the non-constant range shift due to the cumulative nature of range walk tends to move the same scattering points out of the range-cell column (known as range cell migration) and affects the cross-range information extraction process (which, in effect, takes DFTs of each range-cell column). This will generally result in distortion of the ISAR image. The choice of Δf also contributes to the range walk effect. For better range resolution, we require high Δf but range walk will tend to be amplified by higher Δf.

To correct the distortion caused by range cell migration of the scattering points, the phase error due to the target velocity has to be mitigated. The simplest method for eliminating this error is to multiply the sampled output data by an equivalent complex factor (Wehner [4])

$$\varsigma = \exp\left\{ -j2\pi f_i \left[\frac{2\tilde{v}_t}{c} \left(iT_2 + \tau_r + \frac{2\tilde{R}_p}{c} \right) \right] \right\} \qquad (2.28)$$

where $\tilde{v}_t$ and $\tilde{R}_p$ are estimated from the Doppler and range tracking of the sampled output data. This is known as translational motion compensation. However, it is evident from (2.28) that the effectiveness of this kind of compensation relies heavily on the precision of Doppler and range tracking techniques in order to get an accurate estimated of the target range and its radial velocity. Compensation methods get more complex if the target velocity varies significantly within the integration period.

There are many methods today that can yield accurate motion estimation. One of the known methods is the entropy measurement but this method is computationally intensive (Jae and Thomas and Flores [3]). Other techniques

include the Cramer-Rao Burst Derivatives Approach (Jae and Thomas and Flores [3]), the Phase Difference method (Wehner [4]), the least square motion parameter estimation (Jae and Thomas and Flores [3]), and even time-frequency analysis approaches (Jae and Thomas and Flores [3] and Chen [2]).

E. ACHIEVING HIGH CROSS-RANGE RESOLUTION USING SYNTHETIC APERTURE

1. ISAR Theory from an Aperture Viewpoint

The method by which ISAR achieves high cross-range resolution is not much different than that of conventional SAR and, in both cases, the bounds are linked closely to the angular extent over which the radar views the target. For an unfocussed SAR, it is the maximum linear path length before the quadratic phase error becomes significant to create the defocusing effect and degradation of resolution. (This phase error results from the difference between the linear path and the curvature of the range to a point target.) In the case of ISAR, the same behavior holds except that the path length is now a function of the target angular rotation rate and the dwell time (which is also usually the image coherent processing or integration time).

Consider a stationary radar viewing a rotating target (see Figure 5(a)) over an angle segment Ψ (aperture) over the integration period (we assume that the translational motion is perfectly compensated). This geometry can be viewed as equivalent to the radar (like SAR) in motion observing a non-rotating target as it passed the same angle segment as shown in Figure 5(b). We assume that the radar is tracking the target in the far-field so that the angular extent of the aperture, projected as path length, L, is $L << R$. Also, the length of the observed target, y, is generally $y << L$. In such cases, from Figure 5(c), the two-way phase advance of the target scattering point, φ, at azimuth position, ϕ_y, from the radar boresight is

$$\varphi(x) \approx 2k\delta r = \frac{4\pi}{\lambda} x \sin \phi_y \qquad (2.29)$$
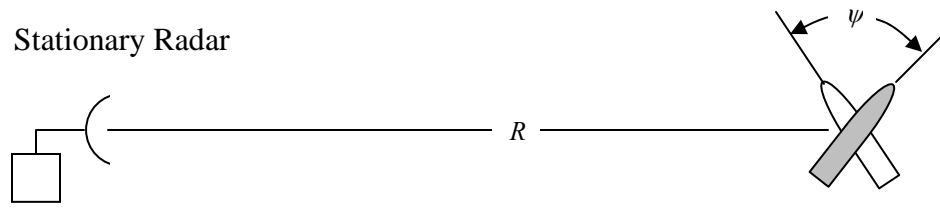
(a) ISAR (After: Figure 7.3(a), pp 344, Wehner [4])
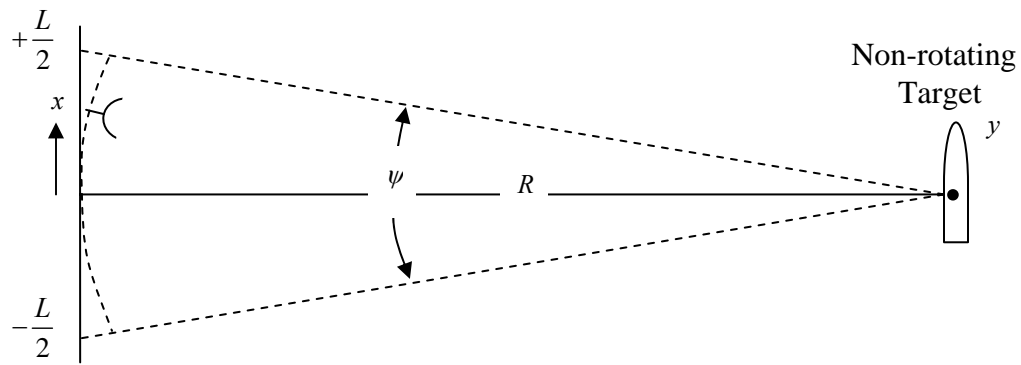
(b) SAR equivalent (After: Figure 7.3(b), pp 344, Wehner [4])
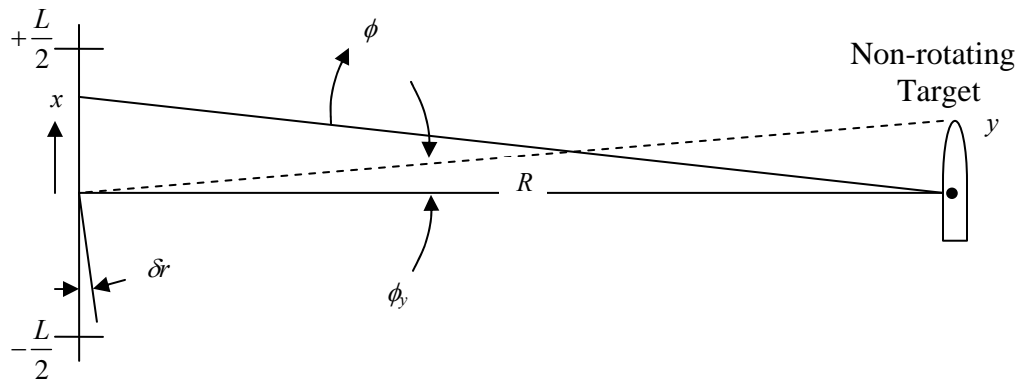
(c) Approximation for $L << R$ and $y << L$ (After: Figure 7.3(c), pp 344, Wehner [4])

Figure 5   SAR and ISAR equivalence.

The term $sin\ \phi_y$ approaches y / R for $y << R$, and the projected length x approaches $R\phi$ under small angle approximation. Hence, (2.29) can be expressed in terms of ϕ and becomes $\varphi(\phi) = 4\pi\ \phi y / \lambda$. Using similar arguments as in linear antenna array theory, the normalized integrated response over the integration angle, Ψ, behaves like a point spread function (PSF) about the cross-range position, y:

$$Z(y) = \int_{-\frac{\psi}{2}}^{\frac{\psi}{2}} \exp\left(j\frac{4\pi}{\lambda}\phi y\right)d\phi = \frac{\sin\left(\frac{2\pi}{\lambda}\psi y\right)}{\frac{2\pi}{\lambda}\psi y}\psi \qquad (2.30)$$

Using the Rayleigh resolution criteria, we can determine the cross-range resolution between two point targets to be $\Delta r_c = \lambda / 2\Psi$. For small integration angle ISAR, we set $\Psi = \omega T$, where ω denotes the target angular rotation rate and T is the integration time. Then, the cross-range resolution is given by

$$\Delta r_c = \frac{\lambda}{2\omega T} \qquad (2.31)$$

Like SAR, the size of the target imposes a maximum allowable Ψ for which this cross-range resolution can be achieved. It can be shown (see Wehner [4]) by setting the maximum allowable phase derivation to be no more than $\pi / 8$ *rad* as the criteria for maintaining focus, that the maximum integration angle before defocusing occurs is

$$\psi_{max} = \frac{1}{2}\sqrt{\frac{\lambda}{\frac{L}{2}}} = \sqrt{\frac{\lambda}{2L}} \qquad (2.32)$$

where the maximum target length is L, and to maintain focus it is necessary that

$$L \leq \frac{(\Delta r_c)^2}{2\lambda} \qquad (2.33)$$

2.   Range Doppler Imaging and Cross Resolution

The cross-range resolution in the above situation is obtained by drawing an analogy to SAR in terms of geometry. The aim is to emphasize the

importance of maintaining a small integration angle, Ψ, within the linear regime for which the quadratic phase is not significant. Unlike SAR, however, in ISAR this angle is affected by the target rotation rate and is often not a known priori — nor can it be generally measured directly by the radar.

In most — if not all — ISAR systems, Doppler processing techniques are directly applied to the signal to obtain the cross-range information. This technique avoids the need for exact knowledge of the target rotation rate, ω, as long as the product of ωT remains within the small integration angle limit. The relationship between target rotation, the point scatterer's cross-range position and its resulting Doppler shift can be understood by referring to Figure 6. If we ignore the Doppler component due to translational motion (it will be shown later that this component is just a linearly added term to the Doppler shift), then the Doppler shift due to the instantaneous velocity of the scattering point at a distance r_c from the center of target, ωr_c, is

$$f_D = \frac{2}{c}\omega r_c f_c = \frac{2\omega r_c}{\lambda}$$ (2.34)
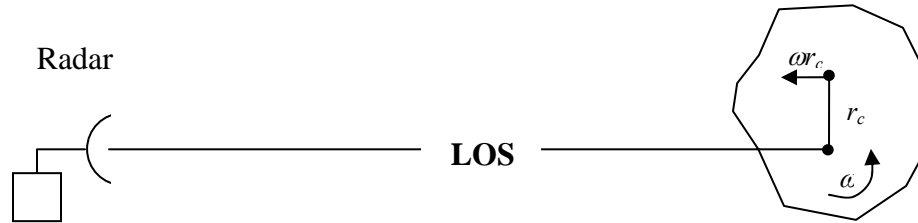
Figure 6   Radial velocity from a point scatterer on a rotating target.
(After: Figure 7.6, pp 351, Wehner [4])

From Equation (2.34) (after some manipulation), the cross-range resolution is seen to be directly related to the Doppler resolution of the radar, Δf_D. Furthermore, since $\Delta f_D = 1/T$, the cross-range resolution can be expressed as

$$\Delta r_c = \frac{\lambda}{2\omega}\Delta f_D = \frac{\lambda}{2\omega T}$$ (2.35)

This expression is the same as that obtained earlier for the cross-range resolution.

3. Doppler Frequency Shift Due to Target Motion

The simple relationships above may not reveal much about the effects of target motion of the ISAR image. To give further insight, let's consider the phase relationship derived earlier in Equation (2.5). An approximation of the Doppler shift induced by the target's motion can be determined by taking the time-derivative of the phase term $\psi(R_{pt})$ where $R_{pt} \cong R(t) + x\cos\theta(t) - y\sin\theta(t)$, $R(t) = R_0 + V_t t + \frac{1}{2}a_t t^2 + ...$ and $\theta(t) = \theta_0 + \omega t + \frac{1}{2}\gamma t^2 + ...$ Neglecting the second order and higher terms of $R(t)$ and $\theta(t)$, we obtain

$$
\begin{aligned}
f_D = \frac{d}{dt}\psi(R_{Pt}) &= \frac{2f_c}{c}V_t + \frac{2f_c}{c}\{-x\omega[\sin\theta_0\cos\omega t + \cos\theta_0\sin\omega t] \\
&\quad -y\omega[\cos\theta_0\cos\omega t + \sin\theta_0\sin\omega t]\} \\
&= f_{DTrans} + f_{DRot}
\end{aligned}
\tag{2.36}
$$

The overall Doppler shift can be seen as a summation of the Doppler shift due to translational motion, $f_{DTrans} = 2f_c V_t / c$, and that due to rotational movement, f_{DRot}, determined by the remaining terms. We can further expand $\sin\omega t = \omega t - \omega^3 t^3 / 6 + ...$ and $\cos\omega t = 1 - \omega^2 t^2 / 2 + ...$ and ignore the higher order terms since the product of both ω and t is generally very small, $\omega^3 t^3 << 1$ and $\omega^2 t^2 << 1$. Thus, f_{DRot} becomes

$$
f_{DRot} = \frac{2f_c}{c}\{-\omega[x\sin\theta_0 + y\cos\theta_0] - \omega^2 t[x\cos\theta_0 - y\sin\theta_0]\}
\tag{2.37}
$$

The first term in (2.37) is used for ISAR imaging. But there exist quadratic phase terms even though the rotation rate remains constant. These quadratic terms vary with time and serve to introduce an additional phase error that can defocus and distort the image during its construction process.

4. Distortion Produced by Target Rotation

Unlike errors due to translational motion, the phase error due to target rotation can cause cell migration in both range and cross-range dimensions and, hence, distortion in the ISAR image. From the 2D radar-target geometry given earlier, cell migration in the range dimension due to target rotation is most significant when the initial target angle is $\theta_0 = \pi / 2$. The number of cells moved in the range dimension over the integration period T is then (following Wehner [4])

$$\Delta M' = abs \frac{1}{\Delta r} \{ R_P(0) - R_P(T) \}$$

$$R_P(t) = R_0 + V_t t + x \cos(\theta_0 + \omega t) - y \sin(\theta_0 + \omega t)$$

(2.38)

To account for time delay shift due to rotation alone, we set $V_t = 0$. Expanding the sine and cosine terms in R_P and setting $\theta_0 = \pi / 2$, we can approximate $\Delta M'$ as

$$\Delta M' = \frac{1}{\Delta r} \{ y - x \sin \omega T - y \cos \omega T \}$$

$$= \frac{1}{\Delta r} \left\{ y - x \left[\omega T - \frac{(\omega T)^3}{6} + ... \right] - y \left[1 - \frac{(\omega T)^2}{2} + ... \right] \right\} \cong \frac{x \omega T}{\Delta r}$$

(2.39)

Cross-range cell migration is most significant when $\theta_0 = 0$. The number of cross-range cells by which the scattering point is offset from its correct position due to target rotation rate over the integration period T is then

$$\Delta M = abs \frac{1}{\Delta f_D} \{ f_{DRot}(0) - f_{DRot}(T) \}$$

(2.40)

Substituting (2.37) into (2.40) and letting $\theta_0 = 0$ and $\Delta f_D = 1 / T$, we get

$$\Delta M \cong \frac{2 f_c (\omega T)^2 x}{c}$$

(2.41)

Earlier, we defined the cross-range resolution as $\Delta r_c = \lambda / 2 \omega T = c / 2 f_c \omega T$, and so by substituting this result into the above equation, we obtain the same expression as in Equation (2.39).

$$\Delta M \cong \frac{x\omega T}{\Delta r_c} \tag{2.42}$$

The extent of the cell migration is dependent on the target size, its rotation rate and the integration time. Also, higher resolution requirements over the same period T would mean increasing the number of range (N) and cross-range cell (M), and a corresponding increase in ΔM and $\Delta M'$. This is similar to the effect of increasing the range resolution discussed in the previous section.

Often, ISAR can be made to remain focused over the entire rotation angle Ψ if the target phase drift in both range and cross-range (also known as blur radius) caused by target rotation is constrained to lie within one cell. From Equation (2.42), if we set $\Delta M \leq 1$ for focused ISAR and for $\omega T = \lambda / 2\Delta r_c$, this yields

$$x \leq \frac{2(\Delta r_c)^2}{\lambda} \tag{2.43}$$

Equation (2.43) is almost the same as Equation (2.33) which was obtained by setting the maximal phase deviation to $\pi / 8$. The equation is determined by "the extremes of the target extent" (Wehner [4]), the required resolution and the frequency used.

THIS PAGE INTENTIONALLY LEFT BLANK

III.   BLAST LOADING ON AIRCRAFT

A.   BLAST IMPACT ON AIRBORNE TARGETS

Explosive munitions, guided or unguided, are extensively used in most weapons today against all kinds of targets: aircrafts, ships, tanks, troops, infrastructures, etc.   These munitions are attractive because of the enormous chemical energy that is released in a very short period when the explosive is detonated.   The huge energy deposited into the medium creates a high velocity high pressure shock front that has damaging effects on the target structure — especially for buildings and fixed infrastructures.   When used against airborne targets, the primary goal is to make use of this high velocity pressure wave to launch small pre-fabricated fragments and shrapnel which will penetrate different parts of the target body, causing a variety of damage mechanisms such as structural tearing, explosion of the fuel tank, loss of flight control and electronics, and injuring or killing the pilot.

Owning to its finite inertial mass, the speed at which these fragments and shrapnel travel will in general be less than the shock-wave speed.   As a consequence, the blast wave will interact with the target body before the fragments and shrapnel arrive.   Most modern airborne targets are constructed from material with tensile strength able to sustain high aerodynamic and environmental drags of flight.   Also, because of the degrees of freedom of the aircraft in air, the net effect of a blast force is more likely to cause translational and rotational motions (as if it is treated as a rigid body) than yielding its structure strength.   A brief impulse moment can thus be captured by ISAR for Battle Damage Assessment (BDA) purposes.

For the fragments and shrapnel that penetrate the target body, different damage mechanisms can occur depending on the nature of the penetration.   If the fragments hit a fuel tank, a secondary explosion will occur and may cause further structural breakup. Alternatively, the fragments may cause the target to lose flight control by damaging the electronics, aero-structures, control

hydraulics, or even killing the pilot. In such cases, the target will display erratic maneuvers. Other scenarios include tearing out the tail and/or the wings, damaging the engine, detonating the weapons stores, etc. Although these effects are also captured by ISAR, they are in general difficult to completely account for even in computer modeling and simulations.

In this thesis, we would like to briefly examine the effects of an explosive blast on the motions of the airborne target and demonstrate how it can be detected using ISAR. These imposed motions are highly dynamic and depend on strength of the explosion, the relative distance and direction in which the detonation occurs, and the surface area of the aircraft subjected to the blast loading. Very often, the solution to these complex motions can not be easily derived analytically. However, numerical solution of these complex equations of motion is possible. Hence, this chapter aims to provide discussions linking the theory of explosive blast in air, the loading of the blast force on the aircraft, and the aircraft's translational and rotational responses through a set of complex equations of motion. In addition, a methodological approach is also proposed to create a computer model to solve these complex equations numerically.

B. CHARACTERISTIC OF EXPLOSIVE BLAST IN AIR
1. Formation of the Blast Wave

Blast waves are formed as a result of the ambient atmosphere being forcibly pushed back by the high pressure gases produced from an explosion. In the initial formation, the shape of the pressure pulse from a conventional chemical explosion is highly dependent on the geometric construction of the explosive charge. However, as the pulses travel in the medium, the higher pressure portions will possess higher speed than the lower pressure parts (Kinney and Graham [10]). Progressively, the wave front becomes steeper as the pressure pulse move out and develops a discontinuity known as an explosive shock as illustrated in Figure 7. Under this condition, increasing amounts of energy will be needed to further alter the shock front shape. The front will largely

remain in this form and acts as an advancing blast wave system propagating away from the charge in the radial direction.
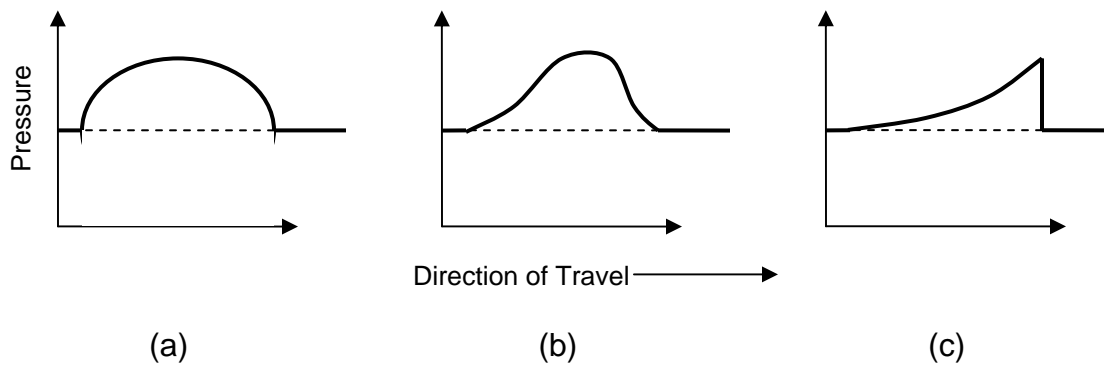
Figure 7   Development of explosive shock. (a) Initial pressure pulse, (b) successive configurations, and (c) Final form when fully developed.
(After: Fig 6-1, pp 89, Kinney and Graham [10])

It is interesting to note that "the fully developed explosive blast-wave system is always formed with about the same general configuration no matter what is assumed for the initial positive pulse. That is, any initial configuration is lost and all blast waves at reasonable distances from the center of an explosion show similar wave forms" (Kinney and Graham [10]).

The amount of energy released by the chemical reaction process from the explosion is an important factor in determine the intensity of the initial shock front and its subsequent impulse shape. In its initial form, the explosion process entails a vanishingly small volume of gases under high pressure. As the gases expand outward, the same amount of energy will need to overcome a larger volume of the atmosphere (which acts to resist the expansion process) hence lowering its resultant shock front intensity and 'stretching' the wave shape as shown in Figure 8.
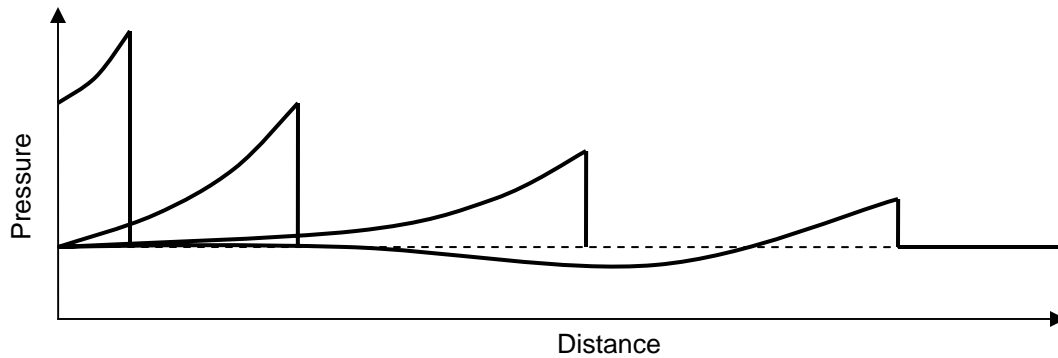
Figure 8   Typical pressure-distance curves for successive times after an explosion.
(After: Fig 6-2, pp 90, Kinney and Graham [10])

At some appreciable distance, the shape of the blast wave will depict a series of positive and negative phases of the pressure. In general, the first positive pressure phase is far more intense in causing damage than the negative ones and its subsequent rarefactions which are limited in magnitude to those of the atmosphere (Kinney and Graham [10]).

2.   Characteristic of the Blast Wave
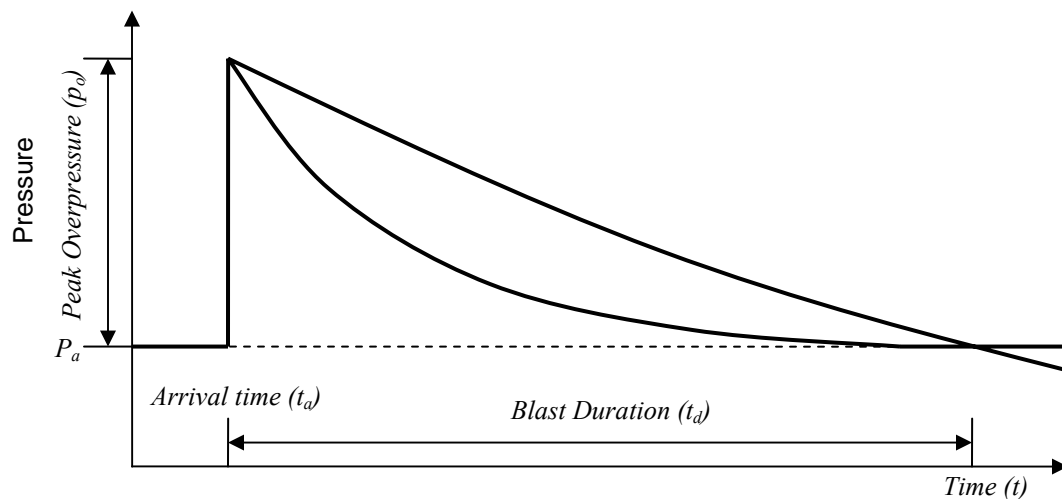
Figure 9   Typical pressure-time curves for explosive blast wave.
(After: Fig 6-5, pp 99, Kinney and Graham [10])

Figure 9 shows a typical pressure-time history characteristic curve of an explosive blast at a certain location away from the center of the explosion (after it is fully developed). At arrival time (t_a) after the explosion, there exists a sudden jump in the pressure intensity (known as peak overpressure) from its atmospheric level. An object at this location will be subjected to an instantaneous lateral force equal to the product of the overpressure and the projected area in the plane of the blast wave. However, this is not a stable condition, and the overpressure at the location will begin to decay exponentially as the volume of gases continues to expand outward, leading to smaller negative and subsequently smaller positive rarefaction phases. For most purposes, the main interest lies in the first positive phase of the blast wave where the damaging effect is considerably more significant than its later ones.

There are four independent parameters that can be used to completely describe the first positive phase of blast wave shape: (a) the initial shock intensity specified by peak overpressure (p_o), (b) the duration of the positive phase of the blast (t_d), (c) the impulse (force-time product) per unit area (I/A), and (d) the arrival time (t_a) which merely introduces an overall time shift of the pressure-time history curve.

An extension of the logarithmic decay expression from Kinney and Graham [10] linking these parameters to the blast wave shape can be given as

$$p(t) = \begin{cases} p_o\left(1 - \dfrac{t-t_a}{t_d}\right)\exp\left[-\dfrac{\alpha(t-t_a)}{t_d}\right] & \text{where} \quad t_a < t < t_d \\ 0 & \text{otherwise} \end{cases} \tag{3.1}$$

where p is the instantaneous overpressure at time t, and α is the waveform parameter related to the impulse per unit area.

3. Peak Overpressure

Theoretical analysis of the peak shock overpressure uses the same approach as for a normal shock. It is, however, complicated by the spherical divergence of the shock front and its transient nature. Both theoretical studies (in some cases, through the use of computer solutions) and experimental measurements are usually correlated to obtain a reasonable expression relating peak intensity to the distance. Following Kinney and Graham [10], the empirically derived peak overpressure-to-distance relationship can be expressed as the ratio of the overpressure to the standard atmospheric pressure of *1013.25mbars* at *15deg C*.

$$\frac{p_o}{P_a} = \frac{798\left[1+\left(\dfrac{Z}{4.5}\right)^2\right]}{\sqrt{1+\left(\dfrac{Z}{0.048}\right)^2}\sqrt{1+\left(\dfrac{Z}{0.32}\right)^2}\sqrt{1+\left(\dfrac{Z}{1.35}\right)^2}} \qquad (3.2)$$

where p_o/P_a is overpressure ratio and Z is the scaled distance of a charge weight at *1kg* TNT equivalent. The scaling of Z to the actual distance will be discussed below.

4. Arrival Time

From Kinney and Graham [10], we noted that the velocity of the shock front is uniquely related to p_o/P_a which in turn depends on the distance between the observed point and the center of the explosion. Hence, given the peak overpressure and the distance over which it occurs, we can obtain the arrival time by noting

$$u_x = \frac{dr}{dt} = a_x M_x \qquad (3.3)$$

where u_x is the shock front velocity, M_x is its Mach number, r is the radial distance, and a_x is the speed of sound in the undisturbed atmosphere. Solving (3.3) by separation of variables and integrating the Mach number from the center

of the charge (assumed to be $rc = 0$) to the distance the shock front arrived, we obtain

$$t_a = \frac{1}{a_x} \int_0^r \frac{1}{M_x} dr \tag{3.4}$$

where the expression for shock velocity in term of Mach number (given by Kinney and Graham [10]) is

$$M_x = 1 + \frac{(k+1)p_o}{2kP_a} \quad \text{where } k = 1.4 \tag{3.5}$$

5.   Blast Duration

The extent of the damage caused by the blast wave is also closely linked to the duration over which the force is applied. Since the impulse (equivalent to the area under the blast wave shape) of the positive phase is much higher than its subsequent phases, it is often used as an index for the blast duration although in "some cases the negative phase duration can be twice as long" (Kinney and Graham [10]). Thus, the blast duration at an observed point is defined to be "the time between the passing of the shock front and the end of the positive pressure phase as marked by a zero overpressure" (Kinney and Graham [10]).

The zero overpressure condition is a characteristic of the sound wave since the shock front velocity will decrease to the speed of sound in the medium. Hence the blast duration is also dependent on the shock velocity. Using a similar approach to that for deriving the arrival time, Kinney and Graham [10] give the relationship between the blast duration and the distance to which the shock front begins to develop as

$$\frac{t_d}{W^{1/3}} = \frac{980\left[1+\left(\dfrac{Z}{0.54}\right)^{10}\right]}{\left[1+\left(\dfrac{Z}{0.02}\right)^3\right]\left[1+\left(\dfrac{Z}{0.74}\right)^6\right]\sqrt{1+\left(\dfrac{Z}{6.9}\right)^2}} \tag{3.6}$$

35

where the term $t_d/W^{1/3}$ is the duration in *msec* for a *1 kg* TNT explosion and *Z* is the same scaled distance as in the peak overpressure expression. The actual blast duration can be obtained by multiplying (3.6) by $W^{1/3}$ where *W* is the weight of the explosive used in *kg*.

6.   Impulse Per Unit Area

Impulse has "the dimensions of the force-time product" and can be obtained graphically from the area under the first positive phase of the blast wave characteristic.   This factor determines the extent of damage to the target structure. From Figure 9, we can see that — apart from the peak overpressure and blast duration — the rate of decay of the overpressure (known as the waveform parameter, α) also affects the amount of impulse force acting on the target. A rapid decay blast wave with the same intensity will have less damaging effect on the target than the slow decaying ones.

However, it is often difficult to determine α from analytical analysis or direct measurement. In contrast, the impulse per unit area (*I/A*) can be easily obtained by experiment, and the empirical relationship between *I/A* and the scaled distance (from Kinney and Graham [10]) can be expressed as

$$I/A = \frac{0.056\sqrt{1+\left(\dfrac{Z}{0.23}\right)^4}}{Z^2 \sqrt[3]{1+\left(\dfrac{Z}{1.55}\right)^3}} \tag{3.7}$$

With Equation (3.7), the waveform parameter in turn can be determined by rearranging the following integral expression

$$I/A = \int_{t_a}^{t_a+t_d} p\,dt = p_o t_d \left[\frac{1}{\alpha} - \frac{1}{\alpha^2}\left(1-e^{-\alpha}\right)\right] \tag{3.8}$$

36

7.   Hopkinson Scaling Law

Scaling of parameters allows the quantitative characteristic of any explosion (especially those drawn from experimental data) to be used for solutions to more general explosive blast wave problems. The scaling law is fundamentally based on the geometrical similarity between the reference and actual object. The general principle for explosive scaling is to consider the two objects to be spherical. Then, by geometry, the ratio of their volumes is proportional to the third power of the ratio of their diameters, and if the two objects have uniform density distribution, their mass ratio also follows the same third power rule.

By extending the above argument, the blast wave of two explosions can be said to be identical if the ratio of their distance is proportional to the cube root of their energy release. If we take the medium into account, it has been shown by Kinney and Graham [10] that the scaling for distance can be expressed as follows:

$$\frac{(actual\_dis\tan ce)(atmospheric\_density)^{1/3}}{(energy\_release)^{1/3}} = (scaled\_dis\tan ce) \qquad (3.9)$$

Since the energy released is related to the velocity of the shock front, which in turn depends on the peak overpressure ratio and hence the atmospheric density, the above expression can be simplified to become

$$Z = (scaled\_dis\tan ce) = \frac{f_d \times (actual\_dis\tan ce)}{W^{1/3}} \qquad (3.10)$$

where f_d is known as the atmospheric transmission factor and accounts for the difference between the actual and standard reference atmosphere (designated by subscript o). f_d can be found using

$$f_d = \left(\frac{\rho}{\rho_o}\right)^{1/3} = \left(\frac{P}{P_o}\right)^{1/3}\left(\frac{T_o}{T}\right)^{1/3} \qquad (3.11)$$

37

The overpressure is indirectly determined by the scaled distance relation, and the actual overpressure is simply

$$Overpressure = overpressure\_ratio \times atmospheric\_pressure \qquad (3.12)$$

This is the situation of the Hopkinson Scaling Law (Ref from Kinney and Graham [10]).

The scaling law for time can also be derived from the scaled to actual distance ratio by noting that the time associated with the blast is the integration of the speed of the blast wave over the distance traveled. Thus, by Kinney and Graham [10], the actual time is related to the scaled time by

$$(actual\_time) = \frac{W^{1/3}(scaled\_time)}{f_t} \qquad (3.13)$$

and f_t is the transmission factor for time taking also into account the ratio between the shock front speed, a, and the sound speed in the medium, a_o. The expression for f_t is given as:

$$f_t = f_d \frac{a}{a_o} = \left(\frac{\rho}{\rho_o}\right)^{1/3}\left(\frac{T}{T_o}\right)^{1/2} = \left(\frac{P}{P_o}\right)^{1/3}\left(\frac{T}{T_o}\right)^{1/6} \qquad (3.14)$$

C.   DYNAMIC LOADING OF BLAST WAVE ON AIRCRAFT
1.   Translational and Rotational Responses
An object placed in the field of an explosive blast wave will experience a dynamic load characterized by the sudden increase in its peak pressure value followed by a gradual decaying process. The net effect depends on the distribution of the pressure wave across the aircraft's surface, which depends on the orientation, geometrical shape and construction of the object, and its resistive forces such as bending moments, drag and aircraft's thrust apart from its inertia. The end result is most likely a non-symmetrical distribution of the pressure intensity across the exposed area and this loading also changes with time. Thus, it is generally a difficult problem to solve analytically.

38

In this thesis, the main interest is to examine the translational and rotational responses of the aircraft as a whole. To accomplish this goal we assume the aircraft to be a rigid body with center of mass located at the origin of the aircraft coordinates (as in Chapter II except that we will expand the case into the third dimension). Consider the geometry of the three dimensional (3D) problem as shown in Figure 10. We assume the blast wave originates from a point source and diverges outward to the target. Different parts of the aircraft surface area exposed to the blast wave will then experience different peak overpressure intensities of different durations and different arrival times (because of their relative distances to the blast point).
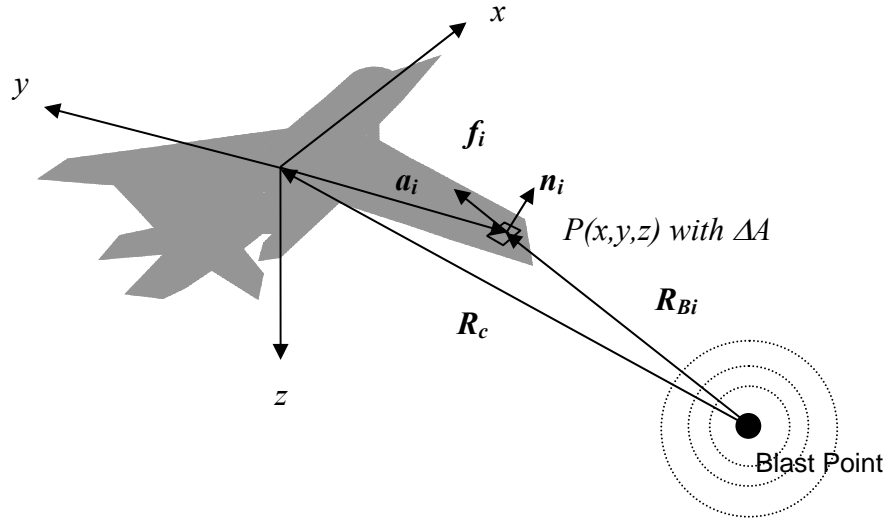
Figure 10   3D geometry of the interaction of blast wave on the aircraft surface.

A directed area element on the aircraft surface at point P can be described by the usual area element (ΔA) and normal vector, n_i, describing the orientation of the aircraft surface. The point P is denoted by the vector a_i. A spherical diverging blast wave will travel in the radial direction along the directed line linking the blast point to the point where the pressure interacts with the target (point P). Denote this vector by R_{Bi}, which can be derived if we know a_i, and the distance between the center of mass of the aircraft and the blast point, denoted

by the vector, R_c. This distance can be taken to be the miss distance of the target (if we assume that the proximity fuse of the explosive munitions triggers at the point where the largest surface area of the target is sensed). The blast wave direction then follows along the direction of R_{Bi} indicated by u_i as

$$u_i = \frac{R_{Bi}}{|R_{Bi}|} = \frac{R_c + a_i}{|R_c + a_i|} \tag{3.15}$$

The elemental force acting at point P is then simply

$$f_i = p_i(t, |R_c + a_i|)\Delta A(n_i \cdot u_i)u_i \tag{3.16}$$

where p_i represents the instantaneous overpressure intensity of the blast wave given in (3.1). Note that p_i is a function of time and distance between point P and the center of the explosion.

It follows that — assuming the aircraft to be a rigid body — the total force, F_B, and moment, M_B, exerted by the blast wave can be expressed in terms of the sum of all the elemental force components over the exposed area of the aircraft body to the blast pressure wave:

$$F_B = \sum_{Exposed\_area} f_i = \sum_{Exposed\_area} p_i(t, |R_c + a_i|)\Delta A(n_i \cdot u_i)u_i \tag{3.17}$$

$$M_B = \sum_{Exposed\_area} a_i \times f_i = \sum_{Exposed\_area} \left[a_i \times p_i(t, |R_c + a_i|)\Delta A(n_i \cdot u_i)u_i\right] \tag{3.18}$$

Since momentum must be conserved in the process, the net effect of the application of these forces over a time increment t gives rise to the changes of both linear and angular momentum (acting on the center and about the center of mass) as follow

$$F_B - Linear\_Resistance = M_G \frac{dv}{dt}$$

$$\int_t (F_B - Linear\_Resistance)dt = M_G[v(t) - v_o] \tag{3.19}$$

$$M_B - Angular\_Resistance = I_G \frac{d\boldsymbol{\omega}}{dt}$$

$$\int_t (M_B - Angular\_Resistance)dt = I_G[\boldsymbol{\omega}(t) - \boldsymbol{\omega}_o]$$

(3.20)

where **Linear_Resistance** and **Angular_Resistance** represent the sum of all the elemental resistive force components. Putting (3.17) and (3.18) into (3.19) and (3.20) respectively and re-arranging them, we can express the variation in linear and angular velocity over time as

$$\boldsymbol{v}(t) = \boldsymbol{v}_o + \frac{1}{M_G} \sum_{Exposed\_area} \int_t p_i(t,| \boldsymbol{R}_c + \boldsymbol{a}_i |)\Delta A(\boldsymbol{n}_i \cdot \boldsymbol{u}_i)\boldsymbol{u}_i dt$$

$$- \frac{1}{M_G} \int_t (\boldsymbol{Linear\_Resistance})dt$$

(3.21)

$$\boldsymbol{\omega}(t) = \boldsymbol{\omega}_o + \frac{1}{I_G} \sum_{Exposed\_area} \int_t [\boldsymbol{a}_i \times p_i(t,| \boldsymbol{R}_c + \boldsymbol{a}_i |)\Delta A(\boldsymbol{n}_i \cdot \boldsymbol{u}_i)\boldsymbol{u}_i]dt$$

$$- \frac{1}{I_G} \int_t (\boldsymbol{Angular\_Resistance})dt$$

(3.22)

The presence of the linear and angular resistive force components add an additional level of complexity when evaluating Equations (3.21) and (3.22). In general, these components vary with time as a result of the aircraft motion. However, even if the resistive component effects can be ignored, the analytical solution to (3.21) and (3.22) is only possible for simple geometrical aircraft shapes (in that we also have to assume that the orientation of the projected area does not change significantly with time due to the aircraft motion). Numerical solution (with the aid of computer simulation) may help to obtain a reasonable estimate of the linear and angular velocity variations for more general shape and different variations. Such simulations can also account for the resistive force components.

2.   Approach to Numerical Simulation for ISAR Imaging

ISAR imaging of an aircraft works by mapping the changes in the phase of the returned signals to the range and cross-range positions of the target scattering centers. Hence, our main interest is to derive from (3.21) and (3.22) the target's radial range and angular position variations that are related to the phases of the returned ISAR signal for image generation.

Consider the following 3D geometry of an ISAR looking at the aircraft as it is being hit by the blast wave.
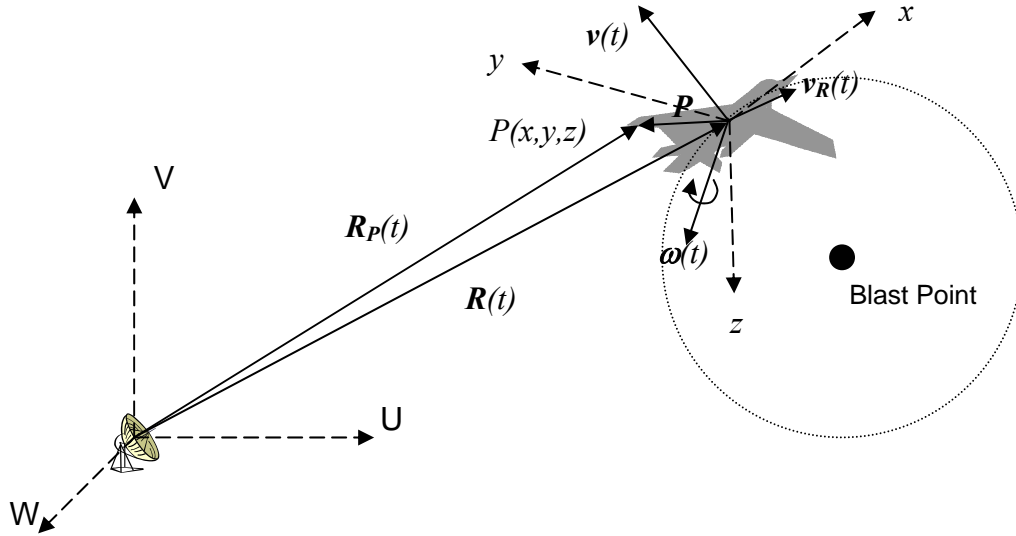
Figure 11   3D geometry of the ISAR staring at aircraft.

From the geometry, the radial velocity detected by the radar can be given by

$$v_R(t) = v(t) \cdot \frac{R(t)}{|R(t)|} \qquad (3.23)$$

Hence, the range, $R(t)$, and angular position, $\theta(t)$ of the target over the entire ISAR coherent integration period, T, can be obtained by integrating (3.23) and (3.22) over T to give

42

$$R(t) = R_0 + \int_T v_R(t)dt = R_0 + \int_T \left[v(t) \cdot \frac{R(t)}{|R(t)|} \right] dt \qquad (3.24)$$

$$\theta(t) = \theta_0 + \int_T |\omega(t)| \, dt \qquad (3.25)$$

From (3.24) and (3.25), we can obtain the range variation of a scattering point on the aircraft (R_P) located at $P(x,y,z)$ (and represented by the vector P) by taking the magnitude of $R(t)$ plus the projection of the vector P onto the fixed radar frame of reference (P is in the aircraft frame of reference and its frame is rotating with time varying θ from the radar frame of reference).

It is not trivial to provide a simple analytical simulation model for (3.24) and (3.25). However, if the distribution of R and θ can be obtained over the integration period T and at intervals equal to the sampling time of the ISAR, S_n, through computer-based simulation, the results of this simulation can be used as inputs to the ISAR radar simulation model to give the solution for R_P (through coordinate transformation and projection). Following the previous discussion, R_P can then be used to map out the ISAR image through Fourier processing. Figure 12 outlines this methodological approach.
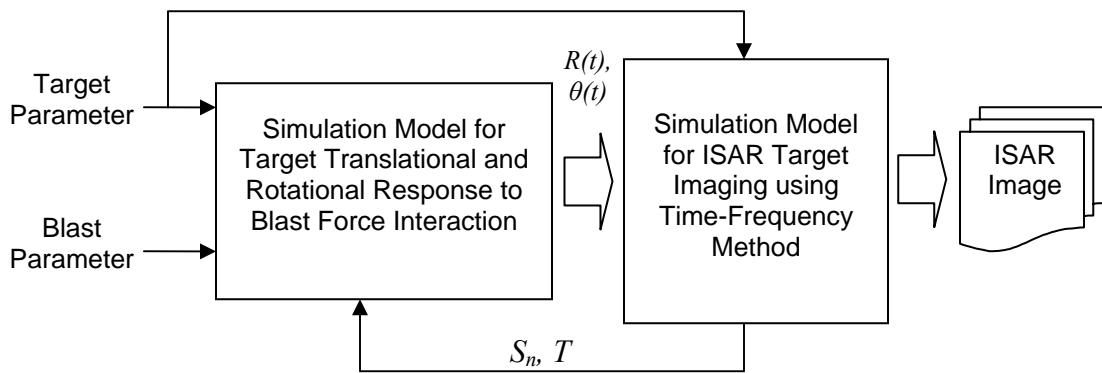
Figure 12   Approach to generate of target motion for ISAR simulation.

In the figure, the block on the left represents the simulation model for solving the equations of motion and provides a stream of R and θ data over the period T with interval to that of S_n. The input to this computer model includes the target parameters (such as its location with respect to the radar, its shape and size, surface orientation, weight and motion), the blast wave parameters, its distance and direction from the target center of mass, the sampling time and the integration period from the ISAR. The output, in term of R and θ together with the target scattering points' locations, is fed into the ISAR simulation model on the right where they are used to generate the ISAR image. A distinct advantage of using this approach is that changes can be made to any one of the models with minimum influence on the others.

D. BLAST WAVE EFFECT ON AIRCRAFT AND ISAR IMAGING

In the development of Chapter II we showed that many ISAR systems rely heavily on the linearity of the target motions (in radial and angular velocity) over the integration period T for radar image generation. This is not desirable for use of ISAR in airborne target Battle Damage Assessment (BDA) since the target is likely to possess high dynamic motions as a result of the blast force interaction with its surface body.

In Equation (3.21) and (3.22), we have shown that these motions contain higher order acceleration components that will alter the phases of the backscattered radar signal in a non-linear manner as it is collected by the radar receiver. Owning to the finite time duration of the blast pressure force, these non-linear components only exist as impulses for a fraction of the time equivalent to blast duration but their magnitude can cause significant changes to the aircraft motion. Also, these impulse forces leave behind residual velocity components for the remaining time of the radar coherent processing period, and are not easily mitigated by motion compensation algorithms. Hence, both the presence of non-linear and residual velocity components will act to interfere with the image processing algorithm and distort the ISAR image.

IV. TIME-FREQUENCY TRANSFORM METHODS OF ISAR IMAGING

A. TIME-FREQUENCY REPRESENTATIONS OF SIGNALS

The Fourier transform is a powerful and widely used method in signal processing and analysis because of its ability to decompose any arbitrary signal into a set of sinusoidal functions with different frequencies. The distribution of frequency components is useful for characterizing the properties and behavior of the signal, and on which signal manipulations such as filtering can be performed to alter them for specific application purposes. However, the Fourier operation and its inverse involve a one-to-one transitional relationship between the time and frequency domains. Consequently, the "information about the time localization of the frequency components" cannot be easily interpreted in the Fourier spectral domain[5] (Hlawatsch and Boudreaux [6]). This limitation is not a problem for stationary types of signals but is generally true for time-varying signal.

Many signals encountered in the real world have frequency content that varies with time. One common example is music where the harmonic content changes for different notes. Other common examples include biomedical signals, speech, vibrations and linear chirp pulses. The time-varying nature of such signal's frequencies makes them rather difficult to represent in the time or frequency domain alone. The time-frequency Transform (TFT) helps to alleviate the situation by mapping a one-dimensional signal as a function of time into a two-dimensional time-frequency plane. Unlike the Fourier transform (which is always linear in nature), the time-frequency representation of the signal can be linear, bi-linear (quadratic) or can contain higher orders of non-linear terms depending on the method of signal representation. In most applications, the first two cases are widely employed and we shall discuss them as follow.

---

[5] Strictly speaking, this information is embedded within the phase of the complex valued frequency components but it is often awkward to operate on in the Fourier domain.

B.   SHORT TIME-FREQUENCY TRANSFORM (STFT)

1.   Definition

The short time-frequency transform (STFT) and its associated Gabor transform are the earliest forms of linear TFT's and date back to the 1940s. In this case, the STFT can be defined as

$$STFT(t,f) = \int s(t')w*(t'-t)e^{-j2\pi ft}dt'$$
(4.1)

where $s(t)$ is the signal and $w*(t)$ is the complex conjugate of an analysis window function with a finite time duration.

From (4.1), the STFT can be seen as taking the Fourier transform of the signal after it is multiplied by the complex conjugate of a shifted window function centered around t. Because the time width of the window function is finite and in general shorter than the signal duration, the effect is the "suppression of the signal outside a neighborhood around the analysis time point $t' = t$." (Hlawatsch and Boudreaux [6]) The STFT represents simply the local spectrum of $s(t')$ at the analysis time t.

The magnitude of the $STFT(t, f)$ is often called the spectrogram of the signal and shows how the frequency spectrum varies as a function of time in the horizontal axis. This magnitude is often represented by a surface above the time-frequency plane and displays the spectral components at that time.

2.   Properties of STFT

According to Hlawatsch and Boudreaux [6], the STFT also has a dual relationship in the frequency domain and can be expressed as

$$STFT(t,f) = e^{-j2\pi ft}\int S(f')W*(f'-f)e^{-j2\pi f't}df'$$
(4.2)

where $S(f)$ and $W(f)$ are the Fourier transform of $s(t)$ and $w(t)$, respectively. This relationship gives additional flexibility in representing the STFT of the same signal from the spectral domain.

There are other important properties of the STFT. The most significant property is that it satisfies the linearity principle where the STFT of the superposition of two signals can be represented by an equivalent linear combination of their respective signals' STFT.

$$s(t) = c_1 s_1(t) + c_2 s_2(t)$$
$$\Rightarrow STFT(t,f) = c_1 STFT_1(t,f) + c_2 STFT_2(t,f) \tag{4.3}$$

The linear behavior of STFT allows the decomposition of a complex signal into a basis set of any arbitrary functions to which the STFT can be easily applied.

Other properties include the preservation of time/frequency under frequency/time shift:

$$s(t) = s_1(t)e^{-j2\pi f_0 t} \Rightarrow STFT(t,f) = STFT_1(t, f - f_0) \tag{4.4}$$

$$s(t) = s_1(t - t_0) \Rightarrow STFT(t,f) = STFT_1(t - t_0, f)e - j2\pi ft_0 \tag{4.5}$$

3.   Time and Frequency Resolution

The time and frequency resolution of the STFT are influenced by the choice of window function and, especially, its width. From (4.1), good time resolution can be achieved using shorter window duration. On the other hand, the dual relationship of Equation (4.2) tells us that a narrow bandwidth is required for good frequency resolution.   But the uncertainty principle of time and frequency in the two domains does not allow the existence of an arbitrarily short time duration and small bandwidth window for the same signal (Hlawatsch and Boudreaux [6]).   Hence, this principle inherently limits the time-frequency resolution of the STFT.

Consider the following two cases (Hlawatsch and Boudreaux [6]). In the first case, we choose the window to be a Dirac delta function with perfect time resolution. Then, for the signal $s(t)$, its STFT is given by

$$STFT(t,f) = \int s(t')\delta(t'-t)e^{-j2\pi ft'}dt' = s(t)e^{-j2\pi ft} \tag{4.6}$$

47

The magnitude is essentially the same as the magnitude of $|s(t)|$ without any information about the frequency content of the signal. Similarly, if we let $W(f) = \delta(f)$ and apply it to (4.2), the STFT of $S(f)$ becomes

$$STFT(t,f) = e^{-j2\pi ft}\int S(f')\delta(f'-f)e^{-j2\pi f't}df' = S(f) \qquad (4.7)$$

which is the Fourier transform of $s(t)$ – its magnitude bears no information about the time variation of the frequency components.

The effect of time and frequency resolution can also be seen by referring to the illustrative example as follows. Figure 14(a) shows a signal whose frequency changes with time and Figure 14(b) is the Fourier transform of this signal. From Figure 14(b), we can see that the frequency domain does not provide any indication on how the signal frequency changes with time.
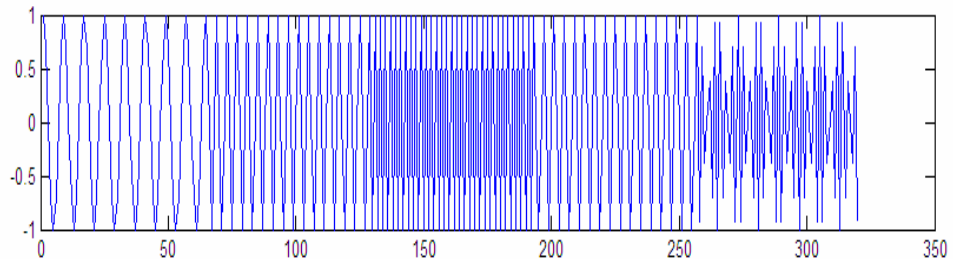
(a) Time Domain Signal
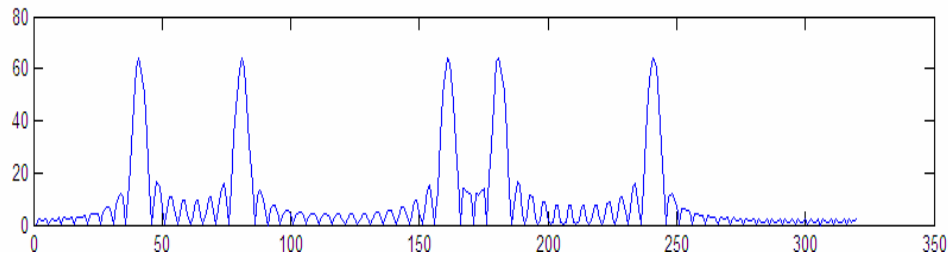
(b) Frequency Domain Representation

Figure 13   Example of a time-varying signal with changing frequency.

The time-frequency representation of the same signal is shown in Figure 14. This figure was generated using a sliding Gaussian window function. In Case 1, we set the width of the window function such that good time resolution can be obtained: notice the significant overlap in frequency. In Case 2, we broaden the window width to give good frequency resolution but in turn the time resolution suffers.
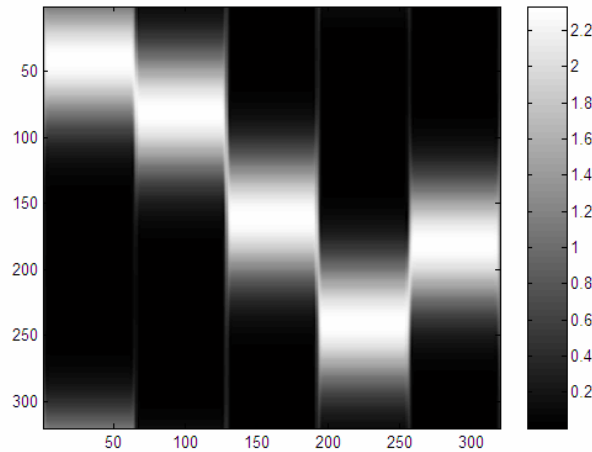
(a) Case 1: Small window size for good time resolution.
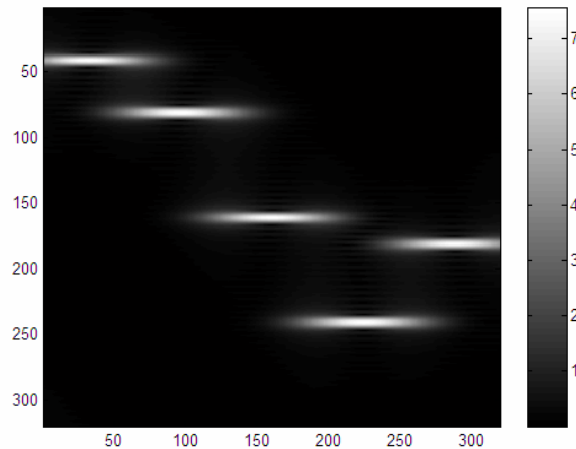
(b) Case 2: Large window size for good frequency resolution.

Figure 14   Effect of Time and frequency resolution.

4.   Shape of the Window Function

The specific shape of the window function is important in reducing the side-lobe interference in the STFT representation. Typically, one requires the window function to taper toward zero smoothly and applies the Hamming, Hanning, Kiaser-Bessel, or Gaussian window function (Chen [2]). The best results have been shown to be achieved by Gaussian windows where the time-bandwidth resolution product is $\Delta t \Delta f = 1/2$ (Refer to Chen [2]). The use of Gaussian windows in an STFT is known as a Gabor transform.

C.   BI-LINEAR TIME-FREQUENCY TRANSFORM

Although the STFT form of signal representations has a nice linear property, the time-frequency resolution is limited by the uncertainty principle, which at best gives a time-bandwidth product of $1/2$. Accordingly, Cohen [12], Hlawatsch and Boudreaux [6] and many others have shown that significant improvement in the time-frequency resolution can be obtained by representing the signal in the quadratic or bi-linear TFT form. The quadratic representation is also "an intuitively reasonable assumption when we want to interpret" the time-frequency of the signal as a form of energy distribution (Hlawatsch and Boudreaux [6]).

To classify a TFT signal representation in the bi-linear form, it must satisfy the following marginal properties related to the energy density.

$$\int TFT(t, f)df = p(t) = |s(t)|^2$$
$$\int TFT(t, f)dt = P(f) = |S(f)|^2$$

(4.8)

where $p(t)$ and $P(f)$ are the instantaneous power and the spectral energy density of the signal $s(t)$ respectively. As a consequence, the signal energy $E = \int |x(t)|^2 dt = \int |X(t)|^2 df$ can be derived by integrating $TFT(t,f)$ over the entire time-frequency plane.

The most difficult part in interpreting the bi-linear TFT representations is the presence of the cross-interference terms which occur as a result of the quadratic superposition principle. Consider the spectrogram of the STFT (which is often loosely interpreted as a bi-linear TFT representation although it does not meet the marginal properties according to Hlawatsch and Boudreaux [6]).

$$SPEC(t,f) = |STFT(t,f)|^2 \tag{4.9}$$

We can easily show that, for the signal $s(t) = s_1(t) + s_2(t)$, the spectrogram of this composite signal is not $SPEC_1(t,f) + SPEC_2(t,f)$ but contains cross interference terms:

$$\begin{aligned} SPEC(t,f) &= |STFT_1(t,f) + STFT_2(t,f)|^2 \\ &= |STFT_1(t,f)|^2 + |STFT_2(t,f)|^2 + 2STFT_1(t,f)STFT_2(t,f) \\ &= SPEC_1(t,f) + SPEC_2(t,f) + Cross\_Intereference \end{aligned} \tag{4.10}$$

This behavior is generally true for all types of bilinear TFT representations although the magnitude of the cross term varies with different types of bi-linear TFT transforms. Also, the more complex the signal is, the more the linear combination of its basis set is used to represent the signal; hence, the more cross interference terms that will appear in the spectrogram and bi-linear TFT representations (Hlawatsch and Boudreaux [6]).

There are many forms of bilinear TFT. The most basic is the Wigner-Ville Distribution (WVD), which is defined as the Fourier transform of the time-dependent autocorrelation of the signal $R(t, t')$ (Chen [2])

$$WVD(t,f) = \int R(t,t')e^{-j2\pi f t'}dt' \tag{4.11}$$

where $R(t, t')$ is chosen as

$$R(t,t') = s\left(t + \frac{t'}{2}\right)s^*\left(t - \frac{t'}{2}\right) \tag{4.12}$$

Because of this relationship with the auto-correlation function, the WVD is known to have very good time-frequency localization and hence good time and

frequency resolution. But this distribution is also known to possess large cross interference terms that hinder its direct usefulness for signal analysis and processing.

A more generalized form known as the "Cohen class" of transforms extends the use of the WVD to include other members of the bilinear TFT representation with a kernel function $\phi(t, t')$. The general form of the Cohen class is given by (Chen [2])

$$C(t,f) = \int\int s\left(u+\frac{t'}{2}\right)s*\left(u-\frac{t'}{2}\right)\phi(t-u,t')e^{-j2\pi ft'}\,du\,dt' \qquad (4.13)$$

Note that the WVD is simply a subset of the Cohen's class with $\phi(t, t') = \delta(t)$. The significance of the Cohen class is that different types of kernel function can be designed to reduce the cross-term interference of the bilinear TFT representation but, in the process, compromise the time-frequency resolution (compared to WVD — which is known (Chen [2]) to possess the best time-frequency resolution). Two well-known distributions in this category are the Choi-Williams distribution (CWD) and the cone-shaped distribution (CSD). Further development of these topics is beyond the scope of this thesis, and we shall not discuss them further. For detailed reviews, refer to excellent texts by Chen [2], Hlawatsch and Boudreaux [6] and Cohen [12].

D. TIME-FREQUENCY BASED IMAGE FORMATION

In Chapter II, we noted the stringent radial and angular motion requirements imposed on ISAR systems for high quality image generation: both velocities must essentially remain constant throughout the coherent integration period. The constant radial velocity allows the radar to accurately estimate the target's linear motion and compensate for it accordingly. To maintain a simple direct relationship for mapping the returned phase variations to the cross-range position of the target's scattering centers, the angular rotation rate must be linear and within an upper bound such that the viewing angle of the ISAR is small enough to prevent cell migration.

However, when the aircraft is being hit by explosive munitions, the blast force will cause changes in both linear and angular momentums. The net effect is that the target will exhibit complex variations in its radial and angular velocities, occurring over a very short time interval (typically, *msec)* and well within the coherent integration time (usually measured in *sec*). Most translational and rotational motion compensation techniques are inadequate to provide good range and Doppler tracking of these complex motions. As a result, the image becomes distorted when conventional Fourier-based techniques are employed for image construction.

The complex variation of the radial and angular velocities from the blast hit can be viewed as a time-varying frequency shift of the returned signals within the integration period. Although these signals pose problems for conventional FFT processing in ISAR systems, the signals do contain information about the dynamic behavior of the aircraft as it is hit, and this information can be extracted using TFT processing.

From an ISAR system architecture point of view, the front end processing remains largely the same. The SFW returned signals are detected and sampled as I- and Q- data, and shipped off to the appropriate range and Doppler tracking algorithm for motion compensation. Synthetic range profile processing is then performed on the $M \times N$ complex-valued sampled data array to obtain the range information as usual. The result is also a $M \times N$ complex-valued matrix array, **H**. Note that, in accordance with our earlier definition, each row of the matrix (denoted as $h(m , 1:N)$ where $m = 1, 2, ..., M$) represents a time-history series comprised of N pulses of range cells. Each column of the matrix (denoted as $h(1:M , n)$ where $n = 1, 2, ..., N$) represents a collection of time-histories of the target from M burst at the particular range cell index n.

In conventional ISAR image processing, the direct Fourier transform (usually implemented by an FFT) is applied to each column $h(1:M , n)$ to obtain the cross-range position of the target scattering points in that range cell index. The Fourier processing still yields a one dimensional column vector:

$$D_{FFT}(1:M,n) = FFT_n\{h(1:M,n)\} \tag{4.14}$$

This process is repeated for all N range cell indices. The result is still a 2D $M \times N$ matrix array with the magnitude of each element indicating the presence of the target point scatterer in the particular range and cross-range positions.

TFT's differ from the conventional Fourier transform method of processing in that the windowed transform (can be linear STFT or bilinear TFT) maps the one-dimensional collection of time-histories of M bursts in each column $h(:,n)$ into a two-dimensional $M \times M$ plane revealing information about the Doppler variation along the time-histories in that cell index.

$$D_{TFT}(1:M,1:M,n) = TFT_n\{h(1:M,n)\} \tag{4.15}$$

This process is repeated for all range cells and we get a *three* dimensional complex-valued array of $M \times M \times N$ Doppler-time-range matrix. Figure 15 depicts the image processing based on TFT method.
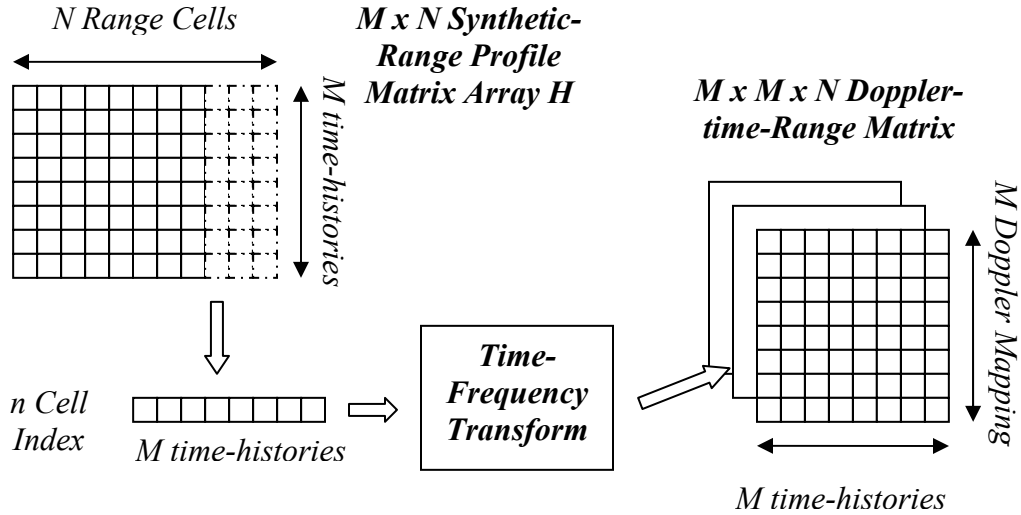
Figure 15   ISAR image processing based of TFT method.

A series of M ISAR images can then be obtained from the three dimensional matrix array by summing over all the range cell indices in each m time-history point as shown in the figure below.

54

M Doppler Mapping from TFT

N Range Cells

M time-histories
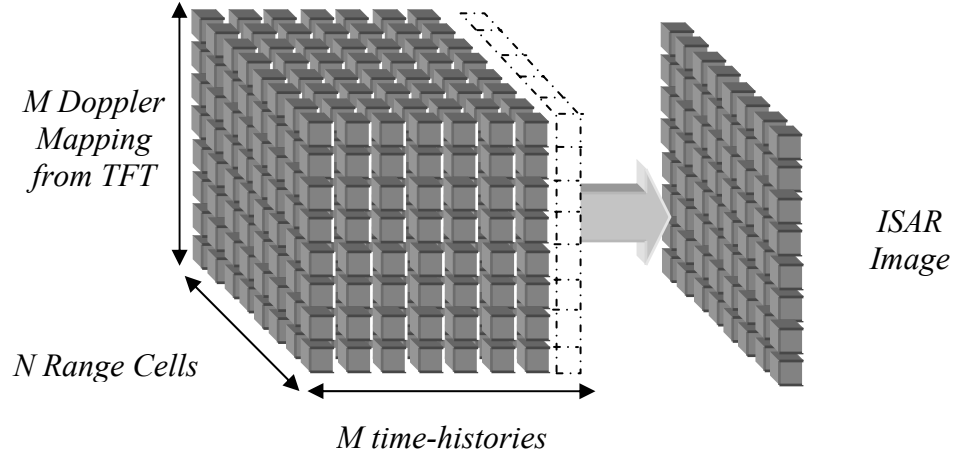
ISAR Image

Figure 16   Extraction of ISAR Image from the Doppler-time-Range Matrix.

The image extraction process can be summarized by the following expression:

$$I_m(1:M,1:N) = D(1:M,m,1:N) \quad \textit{for m = 1, 2, ..., M} \qquad (4.16)$$

When the same process is repeated for each time-history series, the time-history series display of the 2D ISAR image with indices running from *m = 1 to M* is analogous to a moving picture of the aircraft within the integration period (as opposed to the static one by the conventional Fourier-based construction method).   Hence the dynamic motion of the aircraft due to the blast effect is revealed by these sets of ISAR images.

The image resolution from TFT's is generally coarser in comparison to the image obtained by conventional FFT. The resolution also depends on the width and shape of the window function for linear TFT. Bilinear TFT's will give better resolution, but the presence of cross interference terms may act to distort the image.

THIS PAGE INTENTIONALLY LEFT BLANK

V. DEMONSTRATION OF BLAST EFFECT CAPTURINGBY ISAR USING TIME-FREQUENCY TRANSFORM

A. BLAST EFFECTS AND THE ISAR SIMULATION MODEL

To demonstrate the possibility of using Time-Frequency Transform (TFT) methods to 'see' the dynamic behavior of an aircraft target in ISAR imaging, a simple simulation model was developed as part of this thesis. This simulation contains two primary sections following the methodological approach described in Chapter III. The first section aims to simulate the response of the aircraft as the result of a blast hit. The second part of the model extends the usual ISAR imaging simulation model[6] to include a time-frequency method of radar imaging based on the work of Chen [2].

The simple model developed for this demonstration does not provide a complete description of the real world problem at hand involving target BDA. There are several limitations associated with this model that deserve comment:

1)   Only two-dimensional geometries are considered to ease the development and thesis illustration. Nevertheless, one can extend the model to the three-dimensional case with careful considerations about the target roll, pitch and yaw effects, and with some manipulations of the frame of references using matrix transformation and vector operations.

2)   Initially, we shall consider only the translational response of the air target in this demonstration. The model's implementation requires analytical expressions for translational and rotational velocities. It is easier to obtain the translational motions from (3.21) with some reasonable assumptions (as we shall see later). However, the angular dependence in Equation (3.22) contains terms related to the geometrical

---

[6] Some of these models are easily available in or as part of publications related to ISAR imaging in the courtesy of the author (s). For this thesis, we would like to acknowledge that our model is a modified version of the Matlab ISAR simulation program using conventional FFT processing from Jae, Thomas and Flores [3] to help in hastening the model development time compared to starting from scratch.

distribution of the projected aircraft area and the distribution of the pressure wave along its surface that needs to be properly accounted for in order to obtain reasonable estimates of the net effect in angular velocities. There is no simple analytical solution to this problem, and it requires a large scale numerical approach which is beyond the scope of this thesis.

3)   Linear time-frequency transform methods (in particular the Short Time-Frequency Transform or STFT) will be used in this study. The main concern with linear TFT's is the time-frequency resolution, which (at best) gives a time-bandwidth product of only ½. We will have to evaluate its adequacy for our purpose before we proposed further improvements to it.

The code for the simulation program was developed using Matlab 6.5 with time-frequency toolbox provided for by Auger et al [7] & [8] available at http://crttsn.univ-nantes.fr/~auger/tftb.html, Aug 2004. The entire code is given in Appendix A.

B.   SIMULATION OF AIRCRAFT RESPONSE TO BLAST WAVE INTERACTION

The primary goal of this part of the simulation is to obtain the translational motion response of the aircraft from the blast hit. This response appears as a form of variation in range as a function of time and can be derived from the equation of motion for translational motion (3.21) and the blast wave expressions given in (3.1). There are certain assumptions needed in order to simplify the derivation. They are described as follows.

1.   Blast Pressure Distribution on Aircraft

To ease the stringent geometrical requirement of the non-symmetrical aircraft surface, we assume the blast wave to be a plane wave with equal pressure distribution on the exposed area of the aircraft body. The exposed area is also assumed to remain constant with time during the evaluation period. By

ignoring the resistive force components, Equation (3.21) can be re-arranged and simplified to become

$$v(t) = v_o + \frac{1}{M_G} \left(\int_t p(t, R_c) dt \right) \left(\sum_{Exposed\_area} \Delta A \right) (n_i \cdot u_i) u_i$$

$$= v_o + \frac{A_p}{M_G} \left(\int_t p(t, R_c) dt \right) u_i \tag{5.1}$$

where v_o is the initial velocity, M_G is the mass of the aircraft, A_p is the projected area of the aircraft exposed to the blast pressure given by

$$A_p = \left(\sum_{Exposed\_area} \Delta A \right) (n_i \cdot u_i) \tag{5.2}$$

and $p(t, R_c)$ is the instantaneous pressure wave described by Equation (3.1). R_c is factored into the original $p(t)$ since the parameters determining the shape of $p(t)$ — p_o, t_a, t_d and α — are actually dependent on the blast distance, R_c. The unit vector n_i represents the direction of the net blast effect which is normal to the aircraft surface subjected to the blast.

Now that the blast pressure acting on the aircraft body is independent of its direction and that the distance R_c can be taken to have constant value under the planar wave assumption, the impulse response (which is integral of $p(t)$ over time t) can be evaluated separately. If we denote the impulse response of the target by $I(t)$, then

$$I(t) = \int_t p(t', R_c) dt'$$

$$= p_o(R_c) \int_t \left[1 - \frac{t' - t_a(R_c)}{t_d(R_c)} \right] \exp \left\{ -\frac{\alpha(R_c)[t' - t_a(R_c)]}{t_d(R_c)} \right\} dt' \quad \text{where} \quad t_a < t < t_d \tag{5.3}$$

where $p_o(R_c)$, $t_a(R_c)$, $t_d(R_c)$ and $\alpha(R_c)$ can be expressed as a function of the blast distance using the empirical Equations (3.2), (3.4), (3.6) and (3.8) respectively.

We denote p_o' as $p_o(R_c)$, t_a' as $t_a(R_c)$, t_d' as $t_d(R_c)$ and α' as $\alpha(R_c)$. Applying the appropriate boundary conditions, we can obtain the solution for $I(t)$ as

$$I(t) = \begin{cases} 0 & \text{for } t < t_a' \\ p_o'\left\{\dfrac{t_d'}{\alpha'}\left(1-\dfrac{1}{\alpha'}\right)\left(1-e^{-\frac{\alpha'}{t_d'}(t-t_a')}\right)+\dfrac{1}{\alpha'}(t-t_a')e^{-\frac{\alpha'}{t_d'}(t-t_a')}\right\} & \text{for } t_a' < t < t_d' + t_a' \\ p_o'\left\{\dfrac{t_d'}{\alpha'}-\dfrac{t_d'}{\alpha'^2}\left(1-e^{-\alpha'}\right)\right\} & \text{for } t_d' + t_a' < t \end{cases}$$
(5.4)

2.   Geometry of the Problem and its Analytical Solution

We are interested in the radial velocity component since this is detectable by the radar as a Doppler shift. To obtain the radial velocity variation, consider an exaggerated two-dimensional geometry of an ISAR looking at the aircraft while an explosive blast occurs near it as shown in Figure 17.
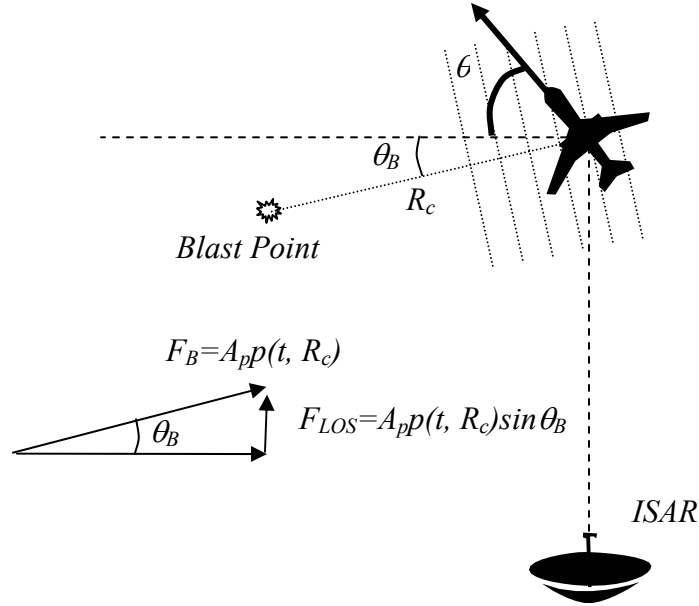
Figure 17   2D Geometry between ISAR, aircraft and blast point.

For the geometry of the figure, the force acting along the radar line-of-sight (LOS) is given by

$$F_{LOS} = A_p p(t, R_c) \sin\theta_B$$
(5.5)

where A_p is the projected surface area of the aircraft to the blast, $p(t, R_c)$ is the instantaneous blast pressure wave as in (3.1), R_c is the blast distance, and θ_B is the direction of the blast wave.

We use the following sign convention: the radial velocity is positive when the target is approaching the radar and negative otherwise. Hence, the resultant radial velocity variation can be simply obtained using conservation of momentum (ignoring all other resistive forces) as follows

$$-\int_t F_{LOS}(t)dt = M_G \left[v_r(t) - v_r(0) \right] \tag{5.6}$$

Re-arranging (5.6) and substituting (5.5) into it, we get

$$\begin{aligned} v_r(t) &= v_r(0) - \frac{A_p \sin \theta_B}{M_G} \int_t p(t, R_c)dt \\ &= v_r(0) - \frac{A_p \sin \theta_B}{M_G} I(t) \end{aligned} \tag{5.7}$$

(Equation (5.7) can also be obtained from the projection of (5.1) onto the radar LOS and the integral is exactly the same as in Equation (5.4).)

For the ISAR simulation model, the target linear motion is expressed as the range variation $R(t)$. To obtain $R(t)$, we simply integrate $v_r(t)$ with respect to time using the following kinematic relationships.

$$\begin{aligned} v_r(t') &= \frac{dR}{dt'} \Rightarrow \int_R dR = \int_t v_r(t')dt' \\ R(t) &= R(0) + \int_t v_r(t')dt' \\ &= R(0) + v_r(0)t - \frac{A_p \sin \theta_B}{M_G} \int_t I(t')dt' \end{aligned} \tag{5.8}$$

The result of the integral $I(t)$ is expressed below, which represents the translational dynamic behavior of the aircraft due to blast effect.

$$R_B(t) = \int_t I(t')dt'$$

$$= \begin{cases} 0 & \text{for } t < t_a' \\[2mm] p_o'\left\{ \dfrac{t_d'^2}{\alpha'^3}(2-\alpha')\left[1-e^{-\frac{\alpha'}{t_d'}(t-t_a')}\right] + \dfrac{t_d'}{\alpha'^2}(t-t_a')\left[\alpha'-1-e^{-\frac{\alpha'}{t_d'}(t-t_a')}\right] \right\} & \text{for } t_a' < t < t_a'+t_d' \\[2mm] p_o'\left\{ C(t_d',t_a',\alpha') - \dfrac{t_d'(1-e^{-\alpha'})}{\alpha'^2}\left[t-(t_a'+t_d')\right] \right\} & \text{for } t_a'+t_d' < t \end{cases} \qquad (5.9)$$

where

$$C(t_d',t_a',\alpha') = \frac{t_d'}{\alpha'} + \frac{t_d'}{\alpha'^2}\left(\alpha'-1-e^{-\alpha'}\right) + \frac{t_d'^2}{\alpha'^3}(2-\alpha')\left[1-e^{-\alpha'}\right] \qquad (5.10)$$

3. Aircraft Profile

Following Equation (5.2), we can define the overall projected area of the aircraft exposed to the blast as the summation of the projected frontal area of its body, A_F, and the projected side area of its body, A_S, and expressed in term of the aircraft's orientation with respect to the blast direction as in Figure 17.

$$A_p = |A_F \cos(\theta_B + \theta)| + |A_S \sin(\theta_B + \theta)| \qquad (5.11)$$

The front and side profiles of the aircraft used in this simulation have a shape shown in Figure 18. Hence, A_F and A_S are given by

$$A_F = \pi \frac{h^2}{4} + (W_s - h)h_W \qquad (5.12)$$
$$A_S = hL + L_T h_T$$
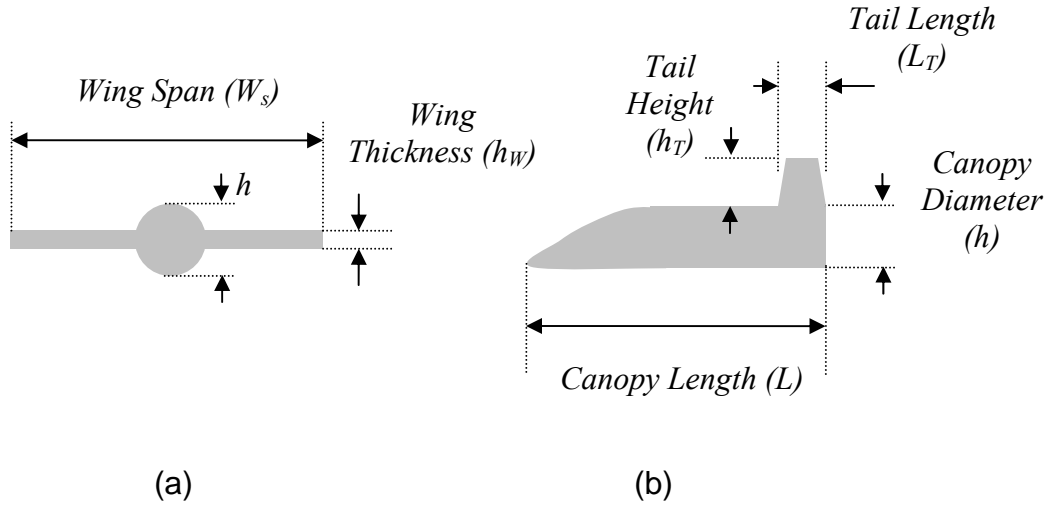
Figure 18   Aircraft area profile.

4.   Blast Parameter

Peak overpressure p_o, arrival time t_a, blast duration t_d and the waveform parameter α are needed to fully describe the blast wave as a function of time. p_o, t_d and α can be easily obtained using the empirical equations given in Chapter III — (3.2), (3.6) and (3.8) respectively. The arrival time t_a, however, requires integration of the speed from the center of explosion to the distance the shock front hits the aircraft. To simplify the simulation, tabulated forms of these data are extracted from Kinney and Graham [10] where they are scaled to *1kg* TNT equivalent values at standard atmospheric pressure and temperature conditions. The actual values can be obtained by using Hopkinson's scaling law described in Chapter III.

For our simulation, the values for the explosive parameters are: explosive weight = 35kg with a TNT equivalent ratio of 1.5 for HE type of explosive. These are figures appropriate to many long range Surface-to-air and Air-to-air missiles. The blast distance is chosen to be 5m, which is within the miss distance of most missiles today.

C. SIMULATION OF ISAR IMAGING USING TIME-FREQUENCY TRANSFORM

The simulation model for generation of the ISAR image consists of three distinct parts: (1) Target model representation, (2) Radar signal generation and (3) ISAR Image processor. The description of each of these portions is as follows.

1. Target Model Representation

It is a common practice in most ISAR simulations to represent the ISAR target as a series of point scatterers outlining the shape of the target. The number of scattering points and the reflectivity of each point can be arbitrary chosen as long as they are within the image plane. For our case, 49 scattering points were used to outline a target and their reflectivity set to one (i.e., uniform signal reflection).

In the model, the target is free to assume any initial orientation with respect to the radar by varying θ_0. The motion for each of the target scattering points is modeled in term of range variation using Equation (2.4), and since the target is treated as a rigid body, the range variation for all the points is influenced by the same kinematic equations for $R(t)$ and $\theta(t)$. The expression used for $R(t)$ follows from the discussion of section (5.8), and $\theta(t)$ is assumed to behave as in Equation (2.3).

2. Radar Signal Generation

The image plane for the ISAR processing is represented by 64 x 64 cell indices — a $N\ x\ M$ matrix array (note that the range and cross-range axis are swapped in this presentation). The radar parameters, f_c, Δf, N pulses, M burst, pulse interval $1/\ PRF$ and integration period T together with the initial range R_0 and rotation rate ω_0 are specifically chosen to optimize the overall radar system such that an ideal image can be obtained without the need to consider range

alignment, range and Doppler tracking, and motion compensation in the process. A summary of these parameters are given in Table 1 below.

The radar signal generation follows the theory in Chapter II and is simply: compute the radial range $R(t)$, angular variation $\theta(t)$ and stepped frequency increases $f_{m,n}$ under (2.8) at each sampling time $t_{m,n}$ in (2.9) for T, and re-arrange them as a N *x* M matrix. These three time-varying matrices are imposed as phases onto the target model and the signal is taken as the sum of these phases from all the scattering points according to (2.10).

Table 1.   Radar Parameters

Parameters	Values	Remarks
Target Initial Rotation Rate, ω	3.77deg/s	Optimized for the target length.
Target Initial Range, R_0	22.567km	Optimized for range alignment.
Carrier Frequency, fc	3GHz	Typical Operating value.
Stepped Frequency, Δf	2.2MHz	Optimized for range resolution.
Number of Pulses, N	64	Arbitrary chosen.
Number of Burst, M	64	Arbitrary chosen.
Pulse Interval, T_2	150μsec	Optimized for Doppler resolution.
Pulse Width, T_1	0.454μsec	$T_1 = 1\,/\,\Delta f$
Integration Period, T	0.6144sec	$T = N\,x\,M\,x\,T_2$
Max Target Length, x	30m	$x = 2(\Delta r_c)^2/\lambda$
Range Resolution, Δr	1.06m	$\Delta r = c/(2N\Delta f)$
Cross-Range Resolution, Δr_c	1.23m	$\Delta r_c = \lambda/(2\omega T)$

3. ISAR Image Processor

The image processing of the radar signal begins by generating the synthetic range profile of the target according to Equation (2.11). Subsequently, the resultant data is passed to another FFT process to construct the conventional two-dimensional mapping of the target image using (2.12).

On the other hand, time-frequency image construction follows the procedures discussed in Chapter IV: the STFT is applied to each row of the $N\,x$ M synthetic range profile matrix as in Equation (4.15). The result is a three-dimensional Doppler-time-range mapping of the target. Each of the M time-histories is then extracted for display accordingly as shown in Figure 16. The operation is carried out using Equation (4.16).

VI. RESULTS AND DISCUSSIONS

A. TIME-FREQUENCY REPRESENTATION OF ISAR IMAGE

(a) Target model.   (b) ISAR image.
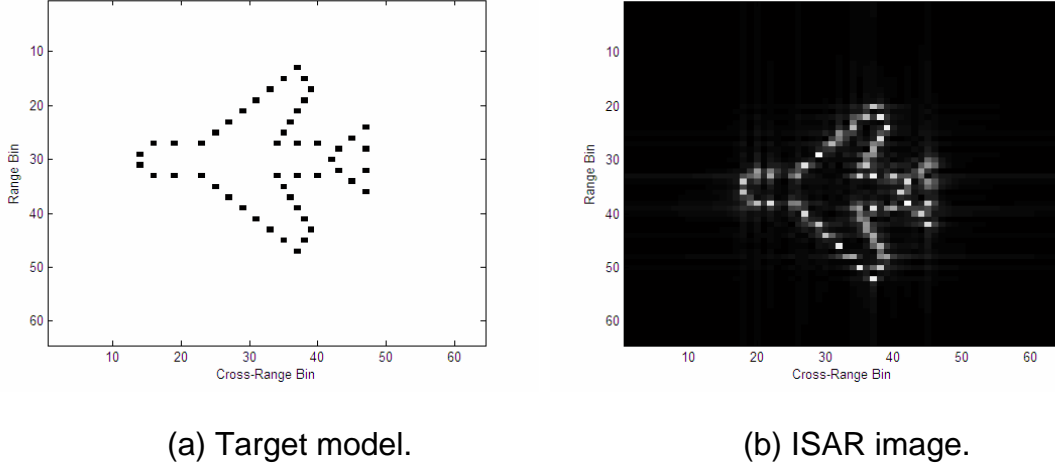
Figure 19   Target model representation and its ISAR Image (from FFT process).

Figure 19(a) above show the model of an aircraft used in this study. The model is represented by the series of 49 point radar scatterers spread over the body length of 35m and wing span of 20m. Figure 19(b) is an ISAR image of the aircraft model generated using the conventional Fourier process (in particular Fast Fourier Transform, FFT) described in Chapter II.

When the same target model is analyzed using the Short Time-Frequency Transform (STFT) method (discussed in Chapter IV), a successive series of 64 time-history ISAR images can be displayed instead. Each of these images shows the same outline of the aircraft image. Figure 20 below shows an example of 16 images extracted from the time-history series of $m = 33$ to 48 (at time t between 0.3168 to $0.4608sec$ where t = 0 indicates the beginning of the coherent processing period).

The image resolution is comparatively poorer — because of the tradeoff in frequency resolution given to the time resolution. Conventional FFT's operate over the entire time-history series of M cells (in our case $M = 64$) but produce

67

only a one-dimensional mapping in the spectral domain. Whereas in STFT, the Fourier processing is carried out with a sliding time window function to yield a two-dimensional time-frequency mapping of each time-history series m where $m = 1, 2, ..., M$. The width of the window is generally chosen to be shorter than M to give better time-resolution, which is important (as we shall see later) for observing the dynamic behavior of the target within the processing period. (In its extreme, we can show that exact FFT image is obtainable from the STFT simply by setting the window width to cover the entire M cells). But the instantaneous frequency resolution suffers as a result, and this frequency is directly related to the cross-range resolution of the ISAR image.

TH33 (t = 0.3168sec)	TH34 (t = 0.3264sec)	TH35 (t = 0.336sec)	TH36 (t = 0.3456sec)
TH37 (t = 0.3552sec)	TH38 (t = 0.3648sec)	TH39 (t = 0.3744sec)	TH40 (t = 0.384sec)
TH41 (t = 0.3936sec)	TH42 (t = 0.4032sec)	TH43 (t = 0.4128sec)	TH44 (t = 0.4224sec)
TH45 (t = 0.432sec)	TH46 (t = 0.4416sec)	TH47 (t = 0.4512sec)	TH48 (t = 0.4608sec)

Figure 20   Sample of ISAR from STFT.

B. TRANSLATIONAL RESPONSE OF AIRCRAFT DUE TO BLAST EFFECT

1. Blast Characteristic

In this study, we place the blast directly between the target and radar along its line-of-sight (LOS) so that the magnitude of translational response will be maximal in the radial direction.   In the first case studied, we only let the side of the aircraft be exposed to the blast wave. The aircraft has a side area of 64m^2 and weight of 22tons.   The translational responses in term of acceleration, velocity and range variation are as shown in Figure 21 and Figure 22.
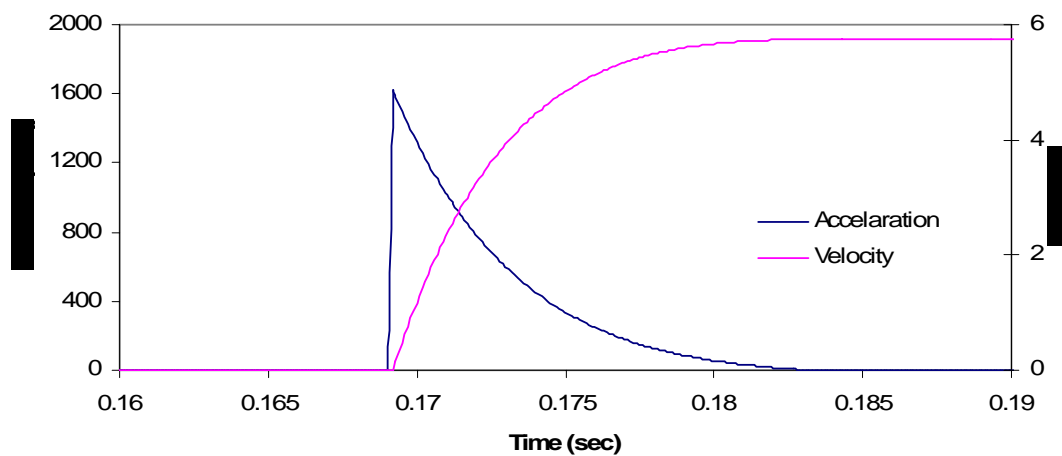
Figure 21   Target acceleration and velocity variation (Blown up version).
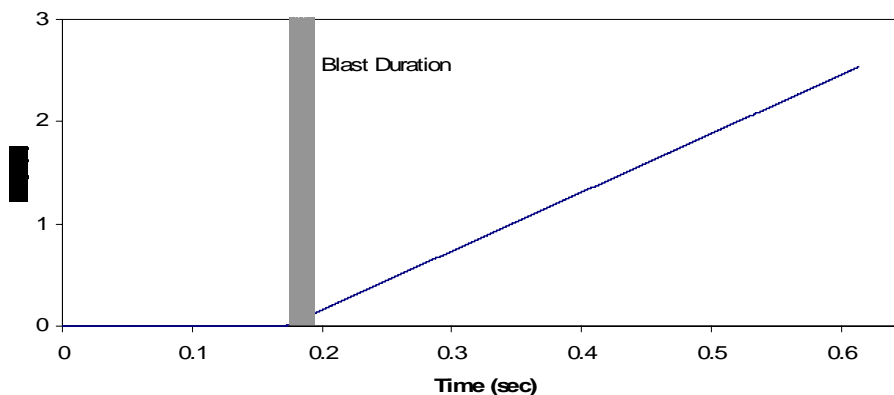
Figure 22   Target range variation.

As expected, the overall acceleration directly follows the impulse response of the blast pressure wave. The presence of this acceleration force gives rise to the non-linear variation in the radial velocity which eventually dissipates away. By conservation of momentum, the change in velocity will cease as the force is taken off the load and is set to a new (constant) value. We note also that the range variation from zero to 3m results from the velocity components. Since these effects happen within one integration period, the ISAR system will not have enough time to compensate for them. Hence the blast effects are effectively introduced as errors in the imaging process.

2.   ISAR Image from Conventional FFT

These errors are manifest as distortions to the radar image as shown in Figure 23(b) when constructed using a conventional FFT. Notice the 'smearing' of the scattering points due to the migration of the range and cross-range cells in the presence of the radial velocity component, and the creation of a seemingly 'double image.' We shall discuss this later when we examine the STFT image. But other than the presence of cell migration, the ISAR image does not reveal anything about the target's behavior within the integration time.
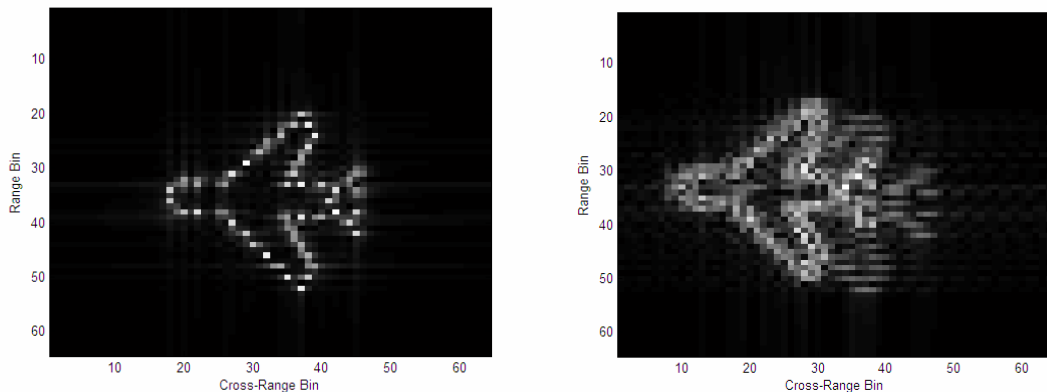
(a) Undistorted.   (b) Distortion due to blast effect.

Figure 23   ISAR image.

3. ISAR Image from STFT

The ISAR images constructed using STFT are shown below in Figure 24. The period of interest is around the time when the blast interaction occurs, which is the first 0.3sec. In the images, we can observe the sequence of events that happen to the aircraft when it is being hit by the blast wave. During the first *0.15sec*, the position of aircraft image is the same as before. As the blast wave arrives, the aircraft image begins to blur because of the velocity variations. This happens for about the same duration as the blast wave interaction with the aircraft body. When the variation stops, the aircraft image becomes gradually clearer (at *t = 0.2sec*) but seems to be offset to a new position, which is an expected effect of a result of the uncompensated velocity components present in the image processing.

(a) At time *t = 0 to 0.1536sec.*

TH17 (t = 0.1632sec)　TH18 (t = 0.1728sec)　TH19 (t = 0.1824sec)　TH20 (t = 0.192sec)

TH21 (t = 0.2016sec)　TH22 (t = 0.2112sec)　TH23 (t = 0.2208sec)　TH24 (t = 0.2304sec)

TH25 (t = 0.24sec)　TH26 (t = 0.2496sec)　TH27 (t = 0.2592sec)　TH28 (t = 0.2688sec)

TH29 (t = 0.2784sec)　TH30 (t = 0.288sec)　TH31 (t = 0.2976sec)　TH32 (t = 0.3072sec)
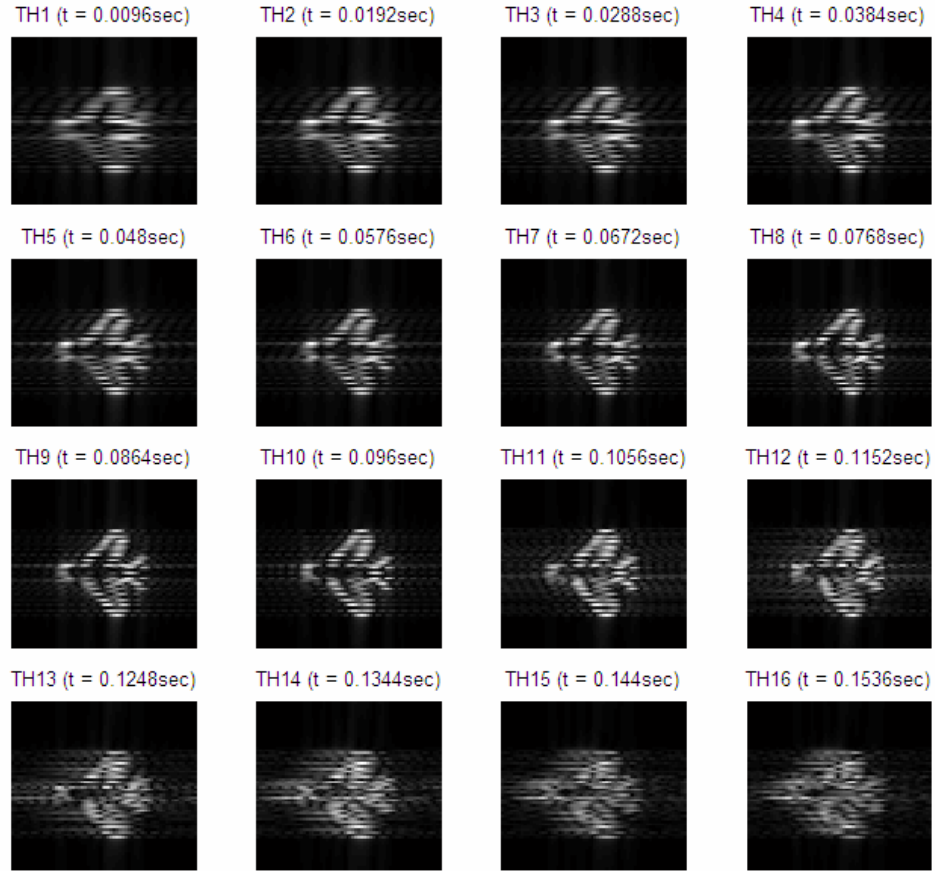
(b) At time $t = 0.1536$ to $0.3072sec$.

Figure 24　STFT ISAR images for observing the blast effect.

From these STFT images, we also make two interesting observations:

1)　　There is a direct correlation with these images to the one obtained using FFT. We notice that the 'smearing' of the image earlier is actually caused by the 'excessive' cell migration from the nonlinear variation of the radial velocity when the blast wave hits the aircraft. Also, the brighter 'double image' is simply the result of continuous imposing of the offset aircraft image after the blast. However, note that the blast has unusually large effect along the cross-range axis rather than the range (The cross-range cell shift is counted to be about 8 – 10 cells whereas the range cell

variation is only 3 cells) although the only velocity component is presence in the radial direction.

2)   The image resolution is much poorer compared to Figure 20. This is a consequence of reducing the size of the window function to only ¼ of the *M* cells so that the time resolution is appropriate to reveal the blast event happening around the time $t = 0.165$ to $0.19sec$. However, we are unable to capture the exact time that the event occurred. Notice that the image blurring begins at $t = 0.1344sec$ and stops only after $t = 0.2016sec$. This is caused by the overlapping of the edges of the window functions at the times when the window is centered in the period that the blast occurs. The time resolution can be improved with shorter window width or sharper cutoff at the edges but such improvement is at the cost of poorer frequency resolution.

These two points shall be discussed in more detail in the later section.

We verify the consistency of the result obtained with a second case in which the orientation of the aircraft is set to face away from the radar and only its back area is subjected to the blast wave. Consequently, the magnitude of the radial velocity variation is reduced from $5.7m/s$ to less than $0.7m/s$. (But the blast characteristic remains the same.)
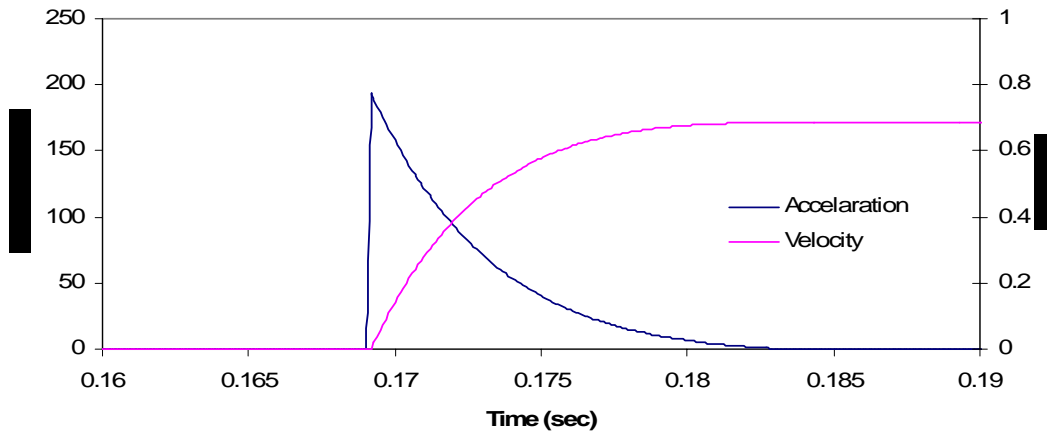
Figure 25   Acceleration and Velocity variation for 2nd case.
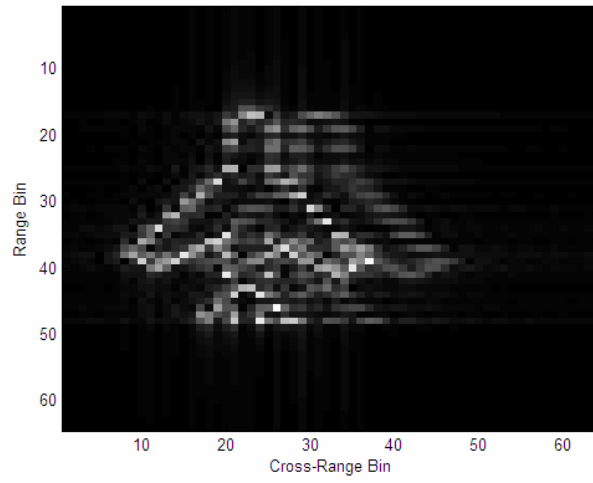
Figure 26   ISAR image from FFT for 2nd Case.

(a) At time *t = 0 to 0.1536sec*.

TH17 (t = 0.1632sec) TH18 (t = 0.1728sec) TH19 (t = 0.1824sec) TH20 (t = 0.192sec)

TH21 (t = 0.2016sec) TH22 (t = 0.2112sec) TH23 (t = 0.2208sec) TH24 (t = 0.2304sec)

TH25 (t = 0.24sec) TH26 (t = 0.2496sec) TH27 (t = 0.2592sec) TH28 (t = 0.2688sec)

TH29 (t = 0.2784sec) TH30 (t = 0.288sec) TH31 (t = 0.2976sec) TH32 (t = 0.3072sec)

(b) At time $t = 0.1536$ to $0.3072sec$.

Figure 27   STFT ISAR images for 2nd case.

Similar cell migration effects are observed in this case, except that the extent of the shift is slightly lessened compared to the first case. This behavior is expected since the velocity variation is lowered in the second case. The cell range-migration is hardly noticeable (virtually zero) whereas the cross-range cell variation is about 6 – 8 cells. Also, the image blurring is less significant in magnitude and duration because of the smaller blast force and shorter blast duration. Other cases were also simulated and examined with different target orientations. Their results, and the associated conclusions, do not differ from those described above.

C.   SELECTION OF WINDOW FUNCTIONS

In the above examples we have seen the important relationship between the time-domain and frequency-domain resolutions (a relationship which, unfortunately, is directly linked to the image quality). For STFT, these resolutions are determined by the size and shape of the window function, and the uncertainty principle associated with the Fourier transform.

1.   Resolution of Rectangular and Gaussian Window Functions

In general, there are numerous window functions to choose from but, for illustration purposes, we will restrict our attention to the two cases for linear TFT's: the simple rectangular function; and the Gaussian function.   The rectangular function can be expressed as

$$w(t) = \begin{cases} 1 & \text{where } -\dfrac{a}{2} < t < \dfrac{a}{2} \\ 0 & \text{otherwise} \end{cases}$$

$$W(f) = a \sin c(\pi a f)$$

(6.1)

where a is the width of the window. And the Gaussian function expression is given by

$$w(t) = \frac{1}{\pi^{1/4} \sqrt{\sigma}} e^{-\frac{t^2}{2\sigma^2}}$$

$$W(f) = (2\sigma)^{1/2} \pi^{1/4} e^{-\frac{\sigma^2 f^2}{2}}$$

(6.2)

The resolutions for the two window functions — in both time and frequency — can be obtained using (Chen [2])

$$\Delta t = \left[\frac{\int_{-\infty}^{\infty} (t - \mu_t)^2 |w(t)|^2 \, dt}{\int_{-\infty}^{\infty} |w(t)|^2 \, dt} \right]^{1/2}, \Delta f = \left[\frac{\int_{-\infty}^{\infty} (f - \mu_f)^2 |W(f)|^2 \, df}{\int_{-\infty}^{\infty} |W(f)|^2 \, df} \right]^{1/2}$$

(6.3)

where

$$\mu_t = \frac{\int\limits_{-\infty}^{\infty} t\,|w(t)|^2\,dt}{\int\limits_{-\infty}^{\infty} |w(t)|^2\,dt}, \mu_f = \frac{\int\limits_{-\infty}^{\infty} f\,|W(f)|^2\,df}{\int\limits_{-\infty}^{\infty} |W(f)|^2\,df}$$

Thus, putting (6.1) into the Equations in (6.3), we derive the time and frequency resolutions for the rectangular function to be $\Delta t = a$, $\Delta f = 1/a$, and its time-bandwidth product $\Delta t \Delta f = 1$. Both resolutions are directly related to the width of the window and multiplicative inverses of each other.

Also, putting (6.2) into (6.3), we obtain for the Gaussian window function, $\Delta t = \sigma/\sqrt{2}$, $\Delta f = 1 / (\sigma\sqrt{2})$ and $\Delta t \Delta f = \frac{1}{2}$. The two resolutions are related to the shape of the window function, which is determined by σ. This gives us an added advantage of stretching the window width to cover the entire time-histories of M cells.

2.   Effect of Using Rectangular Window Function in STFT Imaging

In our earlier demonstration (the first case shown in Figure 24), we used a rectangular window function with a window size $a = \frac{1}{4} \text{ of } 64$ cells $= 16$ cells. The interval between each cell was $N \text{ x } T2 = 64 \text{ x } 150\mu sec = 9.6msec$. By setting the window width to 16 cells, we obtained the resolutions $\Delta t = a = 153.6msec$ and $\Delta f = 1/a = 6.51Hz$.

For that example, the blast event happened between time steps 0.165 and $0.19sec$ and was only $25msec$ in duration. Thus, the selected time resolution is about six times larger than the blast duration. This fact explains why the STFT ISAR image could not faithfully capture the event. The reconstructed images began to mark the blurring effect at $t = 0.096sec$ and end at about $t = 0.2496sec$. The difference of $153.6msec$ is equivalent to the time resolution of the rectangular function. To obtain accurate tracking of the event, the window size should be smaller than $25msec$, which (for our case) is one to two m-cells. But in doing so, the frequency resolution will decline significantly to about $1/a = 1/(2 \text{ x } 9.6msec) =$

52.1Hz. At this frequency resolution, it is virtually impossible to map out the image at all. Below is an example showing the serious degradation of the image by setting the window size to *2 m*-cells.
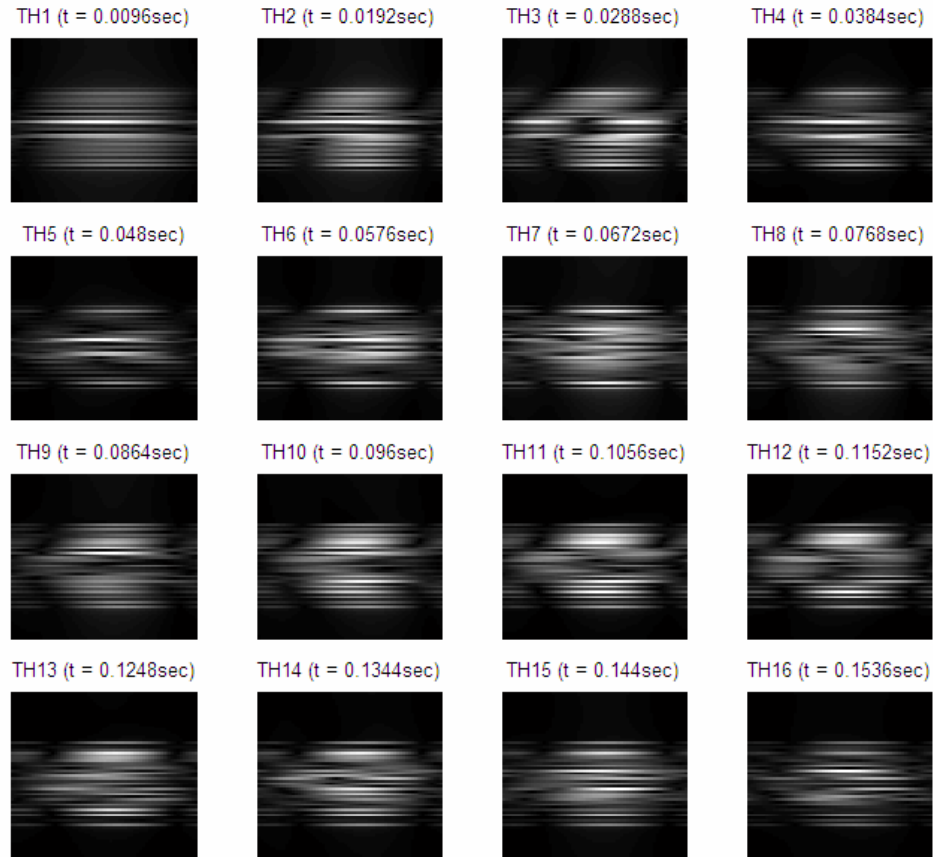
Figure 28   STFT ISAR Time-history images with width set to 2 m-cell.

The Doppler resolution for image quality is inversely proportional to the integration time *T*.   Since *T = 0.6144sec*, we obtain the required frequency resolution to be $\Delta f_D = 1/T = 1.62Hz$.   But the frequency resolution of the above is four times coarser than Δf_D.   As a result, the image quality is generally poorer compared to the conventional FFT ISAR imaging.   We can improve the image quality by extending the window size to ½ of the *M* cells (or more) but that would mean losing the time resolution and the dynamic behavior of the aircraft response could no longer be tracked. An example of this effect, with the window size set to *55 m-cells,* is shown in Figure 29.   Notice that the position offset is

shown right at the start of the integration time while the blast effect occur at $t =$ *0.165sec*. But the quality of the images is better than previous ones.

Figure 29   STFT ISAR Time-history images with width set to 55 m-cell.

3.   Effect of Using Gaussian Window Function in STFT Imaging

Compared to the rectangular window function, the time-bandwidth product of the Gaussian window of only ½ allows better time and frequency resolution to be obtained with lower limits on each. Figure 30 shows a graph comparing the Gaussian and rectangular window function in term of their time versus frequency resolution. The graph is obtained using their respective time-bandwidth product. From the graph, we can easily see that the Gaussian window requires a smaller window size to obtain quality image frequency resolution. Conversely, for the same time resolution it has better frequency resolution than the rectangular function.
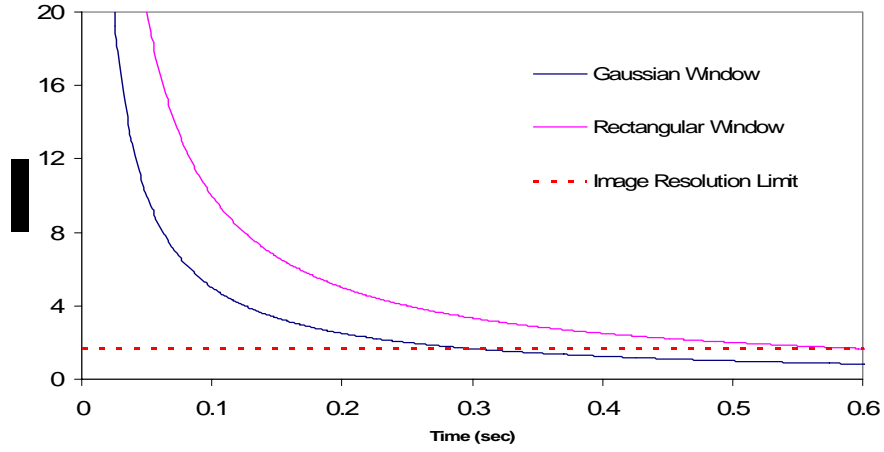
Figure 30 Time and frequency resolution comparison chart for rectangular and Gaussian window functions.

(a) At time *t = 0 to 0.1536sec*.

TH17 (t = 0.1632sec)	TH18 (t = 0.1728sec)	TH19 (t = 0.1824sec)	TH20 (t = 0.192sec)
TH21 (t = 0.2016sec)	TH22 (t = 0.2112sec)	TH23 (t = 0.2208sec)	TH24 (t = 0.2304sec)
TH25 (t = 0.24sec)	TH26 (t = 0.2496sec)	TH27 (t = 0.2592sec)	TH28 (t = 0.2688sec)
TH29 (t = 0.2784sec)	TH30 (t = 0.288sec)	TH31 (t = 0.2976sec)	TH32 (t = 0.3072sec)
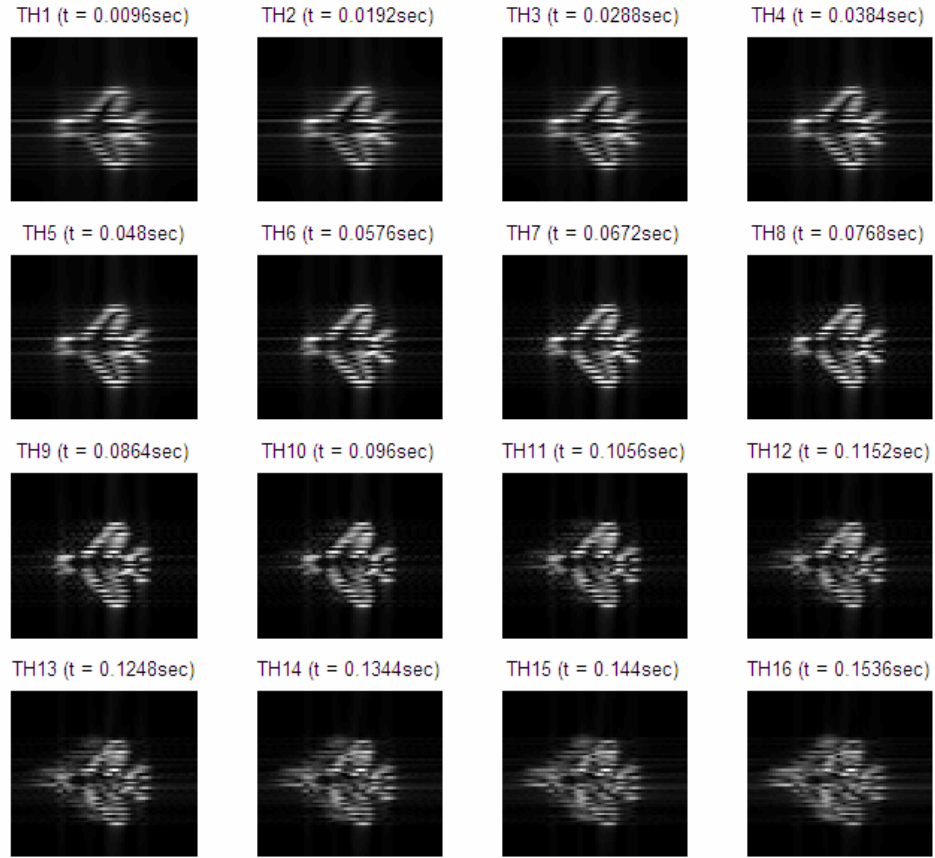
(b) At time $t = 0.1536$ to $0.3072sec$.

Figure 31   STFT ISAR Time-history images with Gaussian window function.

Figure 31 shows the same 32 STFT images generated using the Gaussian window and should be contrasted with the rectangular window used earlier. To enable a direct comparison, we set the time resolution of the Gaussian window to be the same as in the first (rectangular window) case i.e. *16 x 9.6msec = 153.6msec*. Since the time and frequency resolutions are determined by the shape of the window function rather than its width, we use $\sigma = \Delta t \sqrt{2} = 0.2172$ to obtain the corresponding frequency resolution as $\Delta f = 1 / (\sigma \sqrt{2}) = 3.26Hz$. This value is only half of the previous case.

We can see that the time resolution remains the same by observing the blurring effect starting at $t = 0.096sec$ and ended slightly early at t = 0.2208sec. The difference of about 124.8sec is close to the time resolution. However, the images' quality has improved over that of the earlier case (as a result of the finer frequency resolution).

D.   EFFECT OF RADIAL VELOCITY VARIATION ON ISAR IMAGE

In the images obtained using FFT or STFT, cell migration in both range and cross-range directions was quite noticeable — particularly along the cross-range axis. This migration caused the 'smearing' of the image and the blurring effect.

To quantify the extent of the cell migration along the range due to the presence of the radial velocity component, we use the expression (2.27) given in Chapter II to obtain a plot of ΔN versus the radial velocity (Figure 32). For a change in the radial velocity that corresponds to about 4 – 5 m/s in our demonstrated blast characteristic, the estimated shift from Figure 32 below is $\Delta N \cong 4$ range cell. This is about the same amount of range cell shift counted in the ISAR images (which is 3 cells given in the previous section). Surprisingly, it is not a significant contribution to image distortion but only causes a slight 'smearing' along the range cell seen earlier.
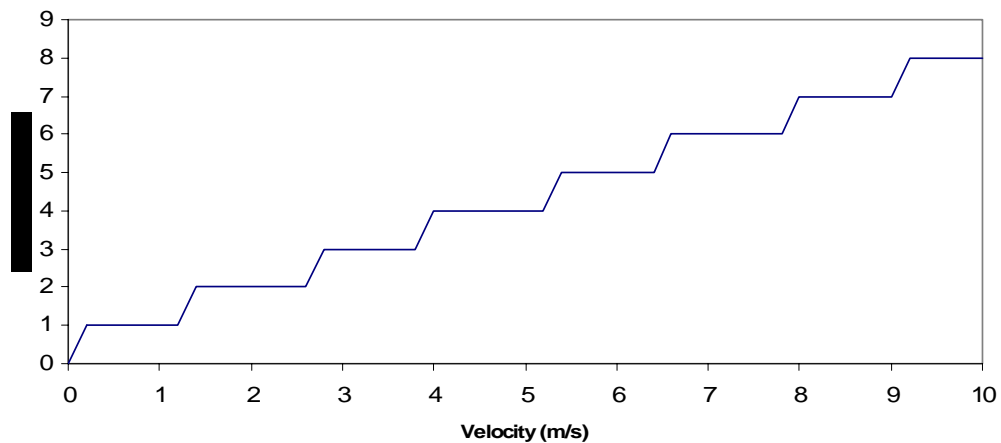

Figure 32   Extent of cell migration due to velocity.

82

Comparatively, cell migration along the cross-range is much higher although there is no angular variation components present in the demonstration. To explain this strange effect, consider the radar signal received within a particular range cell index n given below (Chen [2]).

$$s_R(t)\big|_n = \sum_{k=1}^{M_n} \exp\left\{-j\frac{4\pi f_c}{c}\left[R(t) + x\cos\theta(t) - y_k\sin\theta(t)\right]\right\} \qquad (6.4)$$

where M_n is the total number of scattering points that share the same range, the target aspect angle $\theta(t)$ is expressed similarly to (2.3), and $R(t)$ is given by (5.8) as shown below.

$$\theta(t) = \theta_0 + \omega t + \frac{1}{2}\gamma t^2 + ... \qquad (6.5)$$

$$R(t) = R_0 + V_t - \frac{A_p\sin\theta_B}{M_G}\int_t P(t', R_c)dt' \qquad (6.6)$$

where R_0 is the range at the start of data collection (integration period) and V_t is the initial radial velocity. From Chapter II, the cross-range cell migration is maximal when the initial angle is zero. Setting $\theta_0 = 0$ and assuming that there is no angular acceleration yields $\theta(t) = \omega t$. Substitute (6.6) into (6.4) and, for zero initial velocity (as in our demonstrated case), we get

$$s_R(t)\big|_n = \sum_{k=1}^{M_n} \exp\left\{-j\frac{4\pi f_c}{c}\left[R_0 - \frac{A_p\sin\theta_B}{M_G}\int_t P(t', R_c)dt' + x\cos\omega t - y_k\sin\omega t\right]\right\} (6.7)$$

By expanding $\sin\omega t = \omega t - \omega^3 t^3/6 + ...$ and $\cos\omega t = 1 - \omega^2 t^2/2 + ...$ in (6.7) and ignoring the higher order terms, we obtain

$$s_R(t)\big|_n \cong \sum_{k=1}^{M} \exp\left\{-j\frac{4\pi f_c}{c}\left[(R_0 + x) - y_k\omega t - \frac{A_p\sin\theta_B}{M_G}\int_t P(t', R_c)dt'\right]\right\}$$
$$\cong \sum_{k=1}^{M} \exp\left\{-j2\pi R_k(t)\right\} \qquad (6.8)$$

It is easier to quantify the effect on cross-range cell migration if we consider the case where there is only one scattering point. The Doppler shift in the range cell with index n then can be obtained by differentiating the range related phase terms in (6.8) to give

$$f_{Dn} \cong \frac{d}{dt} R_k(t)$$

$$\cong \frac{d}{dt} \left\{ \frac{2f_c}{c} \left[(R_0 + x) - y_k \omega t - \frac{A_p \sin \theta_B}{M_G} \int_t P(t', R_c) dt' \right] \right\} \qquad (6.9)$$

$$\cong \frac{2f_c}{c} \left[-y_k \omega - \frac{A_p \sin \theta_B}{M_G} P(t, R_c) \right]$$

where

$$P(t) = \begin{cases} 0 & \text{for } t < t_a \\ p_o \left\{ \frac{t_d}{\alpha} \left(1 - \frac{1}{\alpha}\right) \left(1 - e^{-\frac{\alpha}{t_d}(t-t_a)}\right) + \frac{1}{\alpha}(t - t_a) e^{-\frac{\alpha}{t_d}(t-t_a)} \right\} & \text{for } t_a < t < t_d + t_a \quad (6.10) \\ p_o \left\{ \frac{t_d}{\alpha} - \frac{t_d}{\alpha^2} \left(1 - e^{-\alpha}\right) \right\} & \text{for } t_d + t_a < t \end{cases}$$

and p_o, t_d, t_a and α depend on R_c, the distance between the blast point and the center of mass of the aircraft. Note that the second term $A_p \sin \theta_B P(t, R_c) / M_G$ in equation (6.9) represents the impulse response of the aircraft, and since the blast duration is much shorter than the integration period, this term is independent of T. Using Equation (2.40) with $\Delta r_c = c / 2f_c \omega T$, we can estimate the amount of cross-range cell shift to be

$$\Delta M \cong abs \frac{1}{\Delta f_D} \left\{ f_D(0) - f_D(T) \right\}$$

$$\cong abs \frac{1}{\Delta f_D} \left\{ -\frac{2f_c}{c} \frac{A_p \sin \theta_B}{M_G} I / A \right\} \qquad (6.11)$$

$$\cong \frac{1}{\Delta r_c} \left[\frac{A_p \sin \theta_B}{\omega M_G} I / A \right]$$

84

where I/A can be obtained using (3.8) for known p_o, t_d and α. From the simulation parameters given in the program in Appendix A — $p_o = 556274.3N/m^2$, $t_d = 0.0141sec$, $\alpha = 2.53$, we obtain $I/A = 1974.7N\text{-}sec/m^2$.

Also, in the first demonstration case, we have $\Delta r_c = 1.23m$, $A_p = 64m^2$, $\theta_B = -90$, $\omega = 3.77deg/sec = 0.0658rad/sec$, $M_G = 22000kg$. Using Equation (6.11), we get $\Delta M \cong 72\ cells$. This is more than the total number of cells in the cross-range. Hence, the scattering points will crossover into the subsequent time-history series of the image and 'appear' as if they belong the scattering points in that time-history. In this case, $\Delta M - M \cong 72 - 64 = 8\ cells$, which is about the same number of cells that was observed in the first demonstrated case. From Equation (6.11), the extent of the cross-range cell migration seems to depend on the aircraft impulse response to the blast wave. This has been verified also for other blast orientation and lower blast magnitude.

THIS PAGE INTENTIONALLY LEFT BLANK

VII. CONCLUSION AND RECOMMENDATIONS

A. CONCLUSION

The work presented in this thesis is a preliminary demonstration of the possibility of using ISAR to conduct battle damage assessment (BDA) (based on computer simulation). The significant advantage of ISAR — as opposed to other types of sensors — is its ability to produce high resolution target images at greater surveillance ranges than optical systems. With high quality images, the positive evaluation of the extent of the target damage can be quickly made and immediate follow-on action can be taken if required.

However, most ISAR images are generally static in nature and require relatively long processing periods to construct. The quality of the image is often tied to the processing time and the prior conditions associated with the processing. The foremost of these conditions is the assumption that the received radar signal is reflected from a target with only constant angular velocity components (an assumption that is used to map the Doppler variation of the respective scattering points caused by the angular rotation to the cross-range position of the scattering points). The presence of the radial velocities and deviation of the angular rotation rate will lead to image distortion. Unfortunately, these variations cannot be ignored during BDA.

In this study, our main interest is on aircraft. When an aircraft is hit by explosive munitions two distinct behaviors can be observed. First, the blast wave of the explosion will interact with the surface body of the aircraft and cause the aircraft to have translational motion, rotational motion and vibration responses. The characteristics of these responses depend on the magnitude of the blast loading, the orientation of the aircraft surface to the blast wave and the direction of these responses with respect to the ISAR observing the target. Second, most explosive munitions against airborne targets carry pre-fabricated fragments and shrapnel aimed to penetrate the thin layer of the target to cause a variety of damages: from loss of flight control, tearing of structures to fuel tanks and

munitions detonation. The nature of this latter effect is more difficult to account for in simulation.

1.   Approach to Model the Aircraft Response When Hit

Our approach was to examine the response of the aircraft in a deterministic manner by looking at blast loading effect. Even so, there was a need to narrow down the scope of the study to within the time frame of this thesis work and our main focus was solely on the translational and rotational motions of the aircraft. This is a reasonable approach if we consider the aircraft as a rigid body in air. These motions are likely to be the dominant responses apart for the latter effect caused by the fragment penetrations. Besides, they are directly detectable by the ISAR system.

Our simulation begins with the formation of a blast wave in air and requires its characteristic parameters to be understood. They are discussed in the initial sections of Chapter III. It was shown that the blast wave can be represented by an impulse pressure force as a function of time by Equation (3.1) that depends on four key parameters — its peak overpressure, blast duration, arrival time and its waveform parameter. These four parameters are, in turn, dependent on the distance between the center of blast and the point of interaction between the pressure force and the surface. The parameters are usually described using empirical equations.

The overall translational and rotational responses of the aircraft from the blast loading can be derived using the equation of motions (Newton's 2nd law). However, the non-symmetrical geometry of the aircraft surface and the unequal distribution of the blast wave (as a result of its spherical divergence) increase the complexity of the problem and it has been shown in Chapter III that it is difficult to yield an analytical closed-form solution. However, the results of Equations (3.21) and (3.22) can be obtained through the use of extensive numerical simulation. The methodological approach for the simulation was also briefly outlined in the

chapter. Due to the time constraint of this thesis work, we were (regrettably) not able to realize it.

Instead, we simplified the study by modeling the translational response of the aircraft alone. This restriction can be accomplished with reasonable assumptions made concerning the nature of the blast wave and the surface area. We have assumed a planar blast wave with equal pressure distribution across the aircraft body. Also, the surface area of the aircraft during the evaluation period does is assumed to not change with time. These assumptions help to decouple the time and geometrical surface dependent pressure distribution of (3.21) into two separable variables shown in Chapter IV and in (5.1) — both independent of each other. The translational motion can be obtained in terms of radial acceleration, velocity and its resultant range variation with respect to time, by solving (5.1) analytically. However, it is not possible to similarly obtain the angular velocity variation since the resultant changes in angular momentum depend on the differences in pressure distribution across the surface.

2. Approach to Overcome the Image Distortion

The blast loading on the aircraft induces variations in both the radial and angular velocities. The velocity variations are encoded as changes in the Doppler frequencies of each returned scattering signal. This information is captured by the ISAR and use for radar imaging. However, the time resolution (which is equivalent to its integration time) of the conventional Fourier method of image processing is extremely poor and it is difficult to extract the dynamic frequency changes during and after the blast event occurs. As a result, the image becomes distorted due to the inability of the Fourier processing to account for the velocity variations.

On the other hand, the Time-frequency Transform (TFT) method of signal analysis offers an added dimension allowing the signal to be represented as its frequency changes with time. We have shown through the use of a simple TFT method of analysis (which is the Short-time Frequency Transform or STFT) that

the dynamic behavior of the aircraft as it is being hit can be revealed in the ISAR images. The TFT images provide more information about the event than with FFT processing alone. The use of TFT for ISAR imaging is also beneficial to similar future work because of its ability to extract time-varying frequencies since many of these efforts will, in some way or another, involve examining Doppler variations of measured radar signals.

B.   RECOMMENDATIONS FOR FURTHER WORK

Although, the use of ISAR systems with TFT processing has been demonstrated in this thesis for BDA, the simulation model used for proof-of-concept gives only an initial indication of this possibility. Further work is highly recommended to refine the present study in the three major areas discussed below.

1.   Complete Model of the Blast Loading on the Aircraft

In this simulation, only the simplest case — the translational motion of the aircraft — is accounted for. Even then, there were certain assumptions made to reduce the magnitude of the problem so that some rough estimates could be obtained (for example, the possible angular variations were not considered). To enable a complete description of the aircraft response to the blast, there is a need to develop a full model that accounts for all the parameters given in Equations (3.21) and (3.22). It is not an impossible task, but requires careful consideration of the geometry of the problem between the aircraft (its surface distribution and orientation), the location of the blast point and its pressure distribution in time and space, and the position of the observing radar. The problem can also be extended from the present two-dimensional analysis to a real world three-dimensional case (but also with an increasing level of complexity). As discussed in Chapter III, this blast effect model can be developed as a separate model and its results can be simply expressed as a collection of time varying range and angular information over the entire integration period (following the methodological approach proposed).

2.   Study of Target Break Up Process

A further extension of the blast model is to include the target break up process due to the penetration of the fragments into the aircraft. However, the break up process is generally treated statistically and depends on the details of the fragment penetration. As a crude start, we could divide the aircraft into different sections and each section could be driven by different translational and rotational responses induced by the blast effect due to the difference in pressure wave distribution in each section. In this case, a series of range and angular variations for different sections can serve as input to the ISAR imaging model. The ISAR imaging model will then introduce the appropriate phase variations according to the range and angular inputs to respective scatterers categorized by the different sections.

3.   Improving the Time and Frequency Resolution of TFT

While the linear Short-time Frequency Transform (STFT) is the simplest to implement for our demonstration, we have seen that the time and frequency resolutions still lack the sensitivity required to provide faithful tracking of the aircraft dynamic behavior due to blast and simultaneously provide high quality radar imagery. Depending on the choice of the sliding window width and shape, the time-resolution can be adjusted in such a way that the dynamic motion of the target within the integration period can be extracted and tracked. But a major drawback of this approach is that, by gaining time resolution, the frequency resolution will necessarily suffer — and the quality of the image depends on the frequency resolution. This limitation is fundamental and is imposed by the uncertainty principle of time and frequency in any Fourier process. For a linear TFT, the best resolution is achievable using Gaussian window with the time-bandwidth product of ½.

From a system point of view, one can further improve both resolutions by having a greater number of range and cross-range cells to represent the image, although other radar considerations (such as the carrier frequency, pulse interval

91

and frequency step size with respect to the size of the target and its rotation rate) will have to be factored in as they are discussed in Chapter II.

The alternate approach is to work on enhancing TFT image processing. Most efforts involving time-frequency analysis utilize the more complex variations of STFT to overcome the time-frequency resolution limit imposed by the STFT. Examples of some of these TFT schemes include the Continuous Wavelet Transform (CWT), the bilinear Wigner-Ville Distribution (WVD), the Cohen's class series and adaptive time-frequency representations. Many of these TFT approaches have reported better time-bandwidth products and, of these, the WVD seems to give best time-frequency resolution (but at the expense of significant cross interference terms).

APPENDIX A: MATLAB CODES

```
% TFT ISAR IMAGE SIMULATOR
% This program is developed to demonstrate the possibility of reconstructing
% ISAR image using Time-Frequency Transform Method. It can be used for
% viewing the dynamic behaviour of the target due to blast effect.
% It contains 4 parts:
%   a.  Part 1 - Define the radar parameters and Target Model.
%   b.  Part 2 - Generate the blast effect on traslational motion.
%   c.  Part 3 - Creates the returned stepped frequency signal.
%               (This is modified from the original code contained in Jae S. S. et
%                al "Range-Doppler Radar Imaging and Motion Compensation", Norwood, MA,
%                Artech House, 2001).
%   b.  Part 4 - Construct the ISAR Image Using 2D FFT and TFT.
% Assumptions Made: Range aligned. Motion compensated. Zero receiving system delay
% and constant amplitude scatterers (unity).

%%%%%%%%%%%%%%%%%%%%%%%%%%%%%%%%%%%%%%%%%%%
% Clear Memory
%%%%%%%%%%%%%%%%%%%%%%%%%%%%%%%%%%%%%%%%%%%
clear all;  fig_con = 0;


%%%%%%%%%%%%%%%%%%%%%%%%%%%%%%%%%%%%%%%%%%%
% PART 1: Define the radar parameters and Target Model.
%%%%%%%%%%%%%%%%%%%%%%%%%%%%%%%%%%%%%%%%%%%
% Define radar parameters

M = 64;           % Total number of bursts
N = 64;           % Total number of pulses
step_f = 2.2e6;    % Frequency step (Hz)
fc = 3e9;         % Starting frequency (Hz)
Ro = 22567.2;      % Initial range (meters)
Vro = 0;          % Initial translational velocity (m/ses)
Acc_ro = 0;        % Initial translational aceleration (m/sec-sq)
Teta_o = 0;        % Initial angle of rotation (deg)
wo = 3.77;         % Initial angular velocity (deg/sec)
alo = -0.03;        % Initial angular acceleration (deg/sec-sq)
c = 3e8;          % Speed of EM wave (m/sec)
T2 = 150e-6;       % Pulse repetition interval (sec)
T1 = 1/step_f;     % Pulse length (sec)


wo = wo*pi/180;  alo = alo*pi/180;  Teta_o = Teta_o*pi/180;
T1 = 1/step_f;

% Define two dimensional density reflectivity function of Aircraft
% Rows are x and y coordinates,
Tgt_Model = zeros(N,M);

Tgt_Model(29,14)=1;, Tgt_Model(31,14)=1;
Tgt_Model(27,16)=1;, Tgt_Model(33,16)=1;
Tgt_Model(27,19)=1;, Tgt_Model(33,19)=1;
Tgt_Model(27,23)=1;, Tgt_Model(33,23)=1;
Tgt_Model(25,25)=1;, Tgt_Model(35,25)=1;
```

```
Tgt_Model(23,27)=1;, Tgt_Model(37,27)=1;
Tgt_Model(21,29)=1;, Tgt_Model(39,29)=1;
Tgt_Model(19,31)=1;, Tgt_Model(41,31)=1;
Tgt_Model(17,33)=1;, Tgt_Model(43,33)=1;
Tgt_Model(15,35)=1;, Tgt_Model(45,35)=1;
Tgt_Model(13,37)=1;, Tgt_Model(47,37)=1;
Tgt_Model(15,38)=1;, Tgt_Model(45,38)=1;
Tgt_Model(17,39)=1;, Tgt_Model(43,39)=1;
Tgt_Model(19,38)=1;, Tgt_Model(41,38)=1;
Tgt_Model(21,37)=1;, Tgt_Model(39,37)=1;
Tgt_Model(23,36)=1;, Tgt_Model(37,36)=1;
Tgt_Model(25,35)=1;, Tgt_Model(35,35)=1;
Tgt_Model(27,34)=1;, Tgt_Model(33,34)=1;
Tgt_Model(27,37)=1;, Tgt_Model(33,37)=1;
Tgt_Model(27,40)=1;, Tgt_Model(33,40)=1;
Tgt_Model(28,43)=1;, Tgt_Model(32,43)=1;
Tgt_Model(26,45)=1;, Tgt_Model(34,45)=1;
Tgt_Model(24,47)=1;, Tgt_Model(36,47)=1;
Tgt_Model(28,47)=1;, Tgt_Model(32,47)=1;
Tgt_Model(30,42)=1;

fig_con = figure(fig_con+1);
imagesc(-Tgt_Model), colormap(gray)
ylabel('Range Bin'), xlabel('Cross-Range Bin')
title('Density Reflectivity Distribution of the Target Scattering Points')


%%%%%%%%%%%%%%%%%%%%%%%%%%%%%%%%%%%%%%%%%%%%%%
% Part 2: Generate the blast effect on traslational motion.
%%%%%%%%%%%%%%%%%%%%%%%%%%%%%%%%%%%%%%%%%%%%%%


% Aircraft Area Profile - Front and Side
Areafront = 7.6416;  % Front Area in m-sq
Areaside = 64;   % Side Area in m-sq
Mass_Aircraft = 22000; % Mass of Aircraft in kg


% Blast Parameters - Air Explosive Profile.
% Based on Medium Range SAM - Explosive Weight = 35kg, Miss Distance = 5m,
% Target Height = 3000m, TNT Equivalent = 1.5 (HE)
fract = 0.25;
Ar_Delay = fract*N*M*T2;   % Arbitary Delay in fraction of integration time
% Obtain from Excel Table - "Blast Effect Study - Input Parameters.xls"
Po = 556274.3;         % Peak Overpressure in Pa (N/m-sq)
ta = 0.015593 + Ar_Delay;      %arrival time in sec
td = 0.014116;      %blast duration in sec
alpha = 2.53;        %waveform parameter

% Geometry of Blast - Equation (5.10), (5.7), (5.8) & (5.9)
TetaB_deg = -90;       % direction of blast (deg) CW ref to neg. crossrange axis
TetaB = TetaB_deg / 180 * pi;
AreaP = abs(Areafront * cos(TetaB + Teta_o)) + abs(Areaside * sin(TetaB + Teta_o)); % Projected Area
Fyo = Po * AreaP * sin(TetaB);
Ayo = - Fyo / Mass_Aircraft;

% Sampling times Si
% Sik vector of 64x64 elements
i = 1:M*N;
```

```matlab
Sik = (T1/2) + 2*Ro/c + ((i-1)*T2);     % Using Equation (2.9)

% Range Variation ( '1' due to blast effect, '0' linear expression)
With_Blast = 1;     % Blast Switch
if With_Blast        % Using Equation (5.7), (5.8) and (5.9)
   Rik = zeros(1,N*M);
   for vect_index = 1:M*N
      if (Sik(vect_index) <= ta)
         Rik(vect_index) = Ro + Vro*Sik(vect_index);
      elseif (Sik(vect_index) > ta) && (Sik(vect_index) <= (ta + td))
         Rik(vect_index) = Ro + Vro*Sik(vect_index) + Ayo*((td/alpha)^2 * (2/alpha-1)*(1-exp(
                           -alpha*(Sik(vect_index)-ta)/td)) +  td/alpha^2 * (Sik(vect_index)-ta)*(
                           alpha-1- exp(-alpha*(Sik(vect_index)-ta)/ td)));
      else
         Rik(vect_index) = Ro + Vro*Sik(vect_index) + Ayo*((td/alpha - td/alpha^2 * (1 - exp(
                           -alpha)))*(Sik(vect_index) - (ta + td)) + td^2/alpha^3 * (2 - alpha) * (
                           1 - exp(-alpha)) + td^2/alpha^2 * (alpha - 1 - exp(-alpha)));
      end
   end
else
   Rik = Ro + Vro*Sik + 0.5*Acc_ro*Sik.^2;     % Equation (2.2)
end
Rik = reshape(Rik,N,M);

% Angular positions - Equation (2.3)
Tetik = Teta_o + wo*Sik + 0.5*alo*Sik.^2;
Tetik = reshape(Tetik,N,M);

%%%%%%%%%%%%%%%%%%%%%%%%%%%%%%%%%%%%%%%%%%%
% Part 3: Creates the returned stepped frequency signal.
%%%%%%%%%%%%%%%%%%%%%%%%%%%%%%%%%%%%%%%%%%%
% Frequency steps - Equation (2.8)
i = 1:M;
fi1 = fc + (i-1)*step_f; fi = [];
for i = 1:N fi = [fi fi1]; end
clear fi1;
fis = reshape(fi,N,M);

% Create the target image by summing all the returns together.
% Step 1: Find the number of point scatterers on the image
numpo = length(find(Tgt_Model == 1));
[xx yy] = find(Tgt_Model == 1);
pos = 1;
target = zeros(M,N);
% Step 2: Perform the summation - Equation (2.10)
for i = 1:numpo
 target = target + exp(-j*4*pi/c*fis.*Rik).*exp(-j*2*pi*( (xx(pos)-N/2)*2*(fis/c).*cos(Tetik)
        - (yy(pos)-N/2)*2*(fis/c).*sin(Tetik)));
 pos = pos +1;
end

%%%%%%%%%%%%%%%%%%%%%%%%%%%%%%%%%%%%%%%%%%%
% PART 4: Construct the ISAR Image Using 2D FFT and TFT.
%%%%%%%%%%%%%%%%%%%%%%%%%%%%%%%%%%%%%%%%%%%
% TFT Cube Initialisation
stft_cube = zeros([N M N]);     % Instant Frequency-Time History-Range Cell
```

```matlab
% Obtain the Synthetic Range Profile of the target - Equation (2.11)
th_target = fft(target);        % fft on column of matrix


% Construct the Conventional FFT Image - Equation (2.12)
fig_con = figure(fig_con+1);
imagesc(fftshift(abs(fft(th_target.').')));
ylabel('Range Bin')
xlabel('Cross-Range Bin')
colormap(gray);


% Perform TFT on the doppler history of each Range cell index using STFT
% Ref: Chapter IV Section D
% Window function
h = window(45,'gauss',0.005);   % For gauss - need to adjust width according to sigma / 0.005
for vect_index = 1:M
    stft_cube(:,:,vect_index) = tfrstft(th_target(vect_index,:).',1:M,M,h).';
end
% Generate and Plot the Reconstructed ISAR
for vect_index1 = 1:4
    fig_con = figure(fig_con+1);
    for vect_index = 1:16
        fii = fftshift(squeeze(stft_cube(vect_index+(vect_index1-1)*16,:,:)).');
        subplot(4,4,vect_index), imagesc(abs(fii)), colormap(gray);
        THmarker = vect_index+(vect_index1-1)*16;
        title(['TH',num2str(THmarker),' (t = ', num2str(THmarker*T2*N),'sec)']);
        axis off;
    end
end
```

LIST OF REFERENCES

[1]   Borden, B., "Radar Imaging of Airborne Target: A Primer for Applied Mathematicians and Physicists", London, England: Inst. Of Physics Pub., 1999.

[2]   Chen, V. C., Ling, H., "Time-Frequency Transforms For Radar Imaging and Signal Analysis", *Norwood, MA: Artech House*, 2002.

[3]   Jae, S. S., Thomas, G., Flores, B. C., "Range-Doppler Radar Imaging and Motion Compensation", *Norwood, MA: Artech House*, 2001.

[4]   Wehner, D. R., "High-Resolution Radar", 2nd Edition, *Norwood, MA: Artech House*, 1995.

[5]   Mensa, D. L, "High Resolution Radar Imaging", *Dedham, MA: Artech House*, 1981.

[6]   Hlawatsch, F. and Boudreaux, G. F., "Linear and Quadratic Time-Frequency Signal Representation", *IEEE Signal Processing Magazine*, April 1992.

[7]   Auger, F. et al., "Time-Frequency Toolbox for Use with Matlab: Tutorial", *Centre National De La Recherche Scientifique (CNRS) Website*, 1995 – 1996.

[8]   Auger, F. et al., "Time-Frequency Toolbox for Use with Matlab: Reference Guide", *Centre National De La Recherche Scientifique (CNRS) Website*, 1995 – 1996.

[9]   Dantec F. A., "Performance Analysis of a Digital Image Synthesizer as a Counter-measure Against Inverse Synthetic Aperture Radar", *Naval Postgraduate School Student Thesis*, September 2002.

[10]   Kinney, G. F. and Graham, K. J., "Explosive Shocks in Air", 2nd Edition, *New York: Springer-Verlag Inc*, 1985.

[11]   Harrison, H. R. and Nettleton, T., "Principles of Engineering Mechanics", 2nd Edition, *London, England: Edward Arnold*, 1994.

[12]   Cohen, L., "Time-Frequency Distributions – A Review", *Proceeding of the IEEE, Vol 7, No. 77*, July 1989.

[13]   http://www.fas.org, August 2004.

[14]   Gerry, M. J. and Potter, L. C., "A Parametric Model for Synthetic Aperture Radar Measurements", *IEEE Transactions on Antennas and Propagation, Vol 47, No. 7,* July 1999.

[15]   Unzueta, M., Flores, B. C. and Vargas, R., "Two-dimensional polar format algorithm for high-quality radar image formation", *SPIE, Vol 2845,* 1996.

[16]   Wang, Y., Ling, H. and Chen, V. C., "Application of adaptive joint time-frequency processing to ISAR image enhancement and Doppler feature extraction for targets with rotating parts", *Part of SPIE Conference on Radar Processing, Technology and Application III, SPIE, Vol 3462,* July 1998.

[17]   Wang, Y., Ling, H. and Chen, V. C., "Application of adaptive joint time-frequency processing to ISAR image enhancement and Doppler feature extraction for targets with rotating parts", *Part of SPIE Conference on Radar Processing, Technology and Application III, SPIE, Vol 3462,* July 1998.

[18]   Chen, V. C. and Qian, S., "Joint Time-Frequency Transform for Radar Range-Doppler Imaging", *IEEE Transactions on Aerospace and Electronic Systems, Vol 34, Nos. 2,* April 1998.

[19]   Thayaparan, T. and Lampropoulos, G., "A New Approach in Time-Frequency Analysis with Applications to Experimental High Range Resolution Radar Data", *Technical Report, Defence R&D Canada, Ottawa,* November 2003.

[20]   Bao, Z. at el, "Time-Frequency Approaches to ISAR Imaging of Maneuvering Targets and Their Limitations", *IEEE Correspondance,* 2001.

[21]   Wang, G., Xia, X. G. and Chen, V. C., "Signal-to-Noise Ratio Analysis in the Joint Time-Frequency Domain for ISAR Imaging", *Part of SPIE Conference on Radar Processing, Technology and Application III, SPIE, Vol 3462,* July 1998.

[22]   Thomas, G., Liu, K., Cabrera, D. S. and Flores, B. C., "Evaluation of time-frequency filtering for SAR/ISAR motion compensation via instantaneous frequency estimators", *SPIE, Vol 2845,* 1996.

[23]   Thomas, G. and Flores, B. C., "Time-Varying Filters for ISAR Motion Compensation", *Part of SPIE Conference on Radar Processing, Technology and Application III, SPIE, Vol 3462,* July 1998.

[24]   Ling, H. and Li, J., "Application of adaptive joint time-frequency processing to ISAR image formation", *IEEE,* 2000.

[25]   Chen, V. C. and Miceli, W. J., "Simulation of ISAR imaging of moving tagets", *IEE Proceeding – Radar, Sonar Navigation, Vol 148, Nos 3,* June 2001.

INITIAL DISTRIBUTION LIST

1.   Defense Technical Information Center
       Ft. Belvoir, Virginia

2.   Dudley Knox Library
       Naval Postgraduate School
       Monterey, California

3.   Chairman, Physics Department, Code PH/Lj
       Naval Postgraduate School
       Monterey, California

4.   Professor Brett H. Borden, Code PH/Bb
       Department of Physics
       Naval Postgraduate School
       Monterey, California

5.   Professor Donald L. Walters, Code PH/We
       Department of Physics
       Naval Postgraduate School
       Monterey, California

6.   Professor Ronald Brown, Code PH/
       Department of Physics
       Naval Postgraduate School
       Monterey, California

7.   Director, Temasek Defence Systems Institute (TDSI)
       Professor Yeo Tat Soon
       National University of Singapore
       Singapore

8.   Lim Kian Guan
       Republic of Singapore Navy
       Singapore